Published in final edited form as:
Nanomedicine (Lond). 2019 March 01; 14(6): 727–752. doi:10.2217/nnm-2018-0436.

Nutlin-loaded magnetic solid lipid nanoparticles for targeted glioblastoma treatment

Agostina Grillone[*,1], **Matteo Battaglini**[**,1,2], **Stefania Moscato**[3], **Letizia Mattii**[3], **César de Julián Fernández**[4], **Alice Scarpellini**[5], **Mario Giorgi**[6], **Edoardo Sinibaldi**[***,7], **Gianni Ciofani**[****,1,8]

[1]Smart Bio-Interfaces, Istituto Italiano di Tecnologia, Viale Rinado Piaggio 34, 56025 Pontedera, Italy

[2]The Biorobotics Institute, Scuola Superiore Sant'Anna, Viale Rinaldo Piaggio 34, 56025 Pontedera, Italy

[3]Department of Clinical & Experimental Medicine, Università di Pisa, Via Savi 10, 56126 Pisa, Italy

[4]Institute of Materials for Electronics & Magnetism, Consiglio Nazionale delle Ricerche-CNR, Parco area delle Scienza 37/A, 43124 Parma, Italy

[5]Electron Microscopy Facility, Istituto Italiano di Tecnologia, Via Morego 30, 16163 Genova, Italy

[6]Veterinary Clinics Department, Università di Pisa, Via Livornese 1, 56010 San Piero a Grado, Italy

[7]Center for Micro-BioRobotics, Istituto Italiano di Tecnologia, Viale Rinaldo Piaggio 34, 56025 Pontedera, Italy

[8]Department of Mechanical & Aerospace Engineering, Politecnico di Torino, Corso Duca degli Abruzzi 24, 10129 Torino, Italy

Abstract

[*]Author for correspondence: agostina.grillone@iit.it. [**]Author for correspondence: matteo.battaglini@iit.it. [***]Author for correspondence: edoardo.sinibaldi@iit.it. [****]Author for correspondence: gianni.ciofani@iit.it.

Author contributions

A Grillone, M Battaglini and G Ciofani conceived the experiments. A Grillone, M Battaglini, S Moscato and L Mattii performed experiments. CDJ Ferna´ ndez performed magnetic characterization. A Scarpellini performed electron microscopy imaging. M Giorgi performed HPLC analysis. E Sinibaldi carried out physical modeling of the system. A Grillone, M Battaglini and G Ciofani wrote the manuscript.

Financial & competing interests disclosure

This work has received funding from the European Research Council (ERC) under the European Union's Horizon 2020 research and innovation program (grant number N° 709613, SLaMM). The authors have no other relevant affiliations or financial involvement with any organization or entity with a financial interest in or financial conflict with the subject matter or materials discussed in the manuscript apart from those disclosed.

No writing assistance was utilized in the production of this manuscript.

Europe PMC Funders Author Manuscripts

Aim—Glioblastoma multiforme is one of the deadliest forms of cancer, and current treatments are limited to palliative cares. The present study proposes a nanotechnology-based solution able to improve both drug efficacy and its delivery efficiency.

Materials & methods—Nutlin-3a and superparamagnetic nanoparticles were encapsulated in solid lipid nanoparticles, and the obtained nanovectors (nutlin-loaded magnetic solid lipid nanoparticle [Nut-Mag-SLNs]) were characterized by analyzing both their physicochemical properties and their effects on U-87 MG glioblastoma cells.

Results—Nut-Mag-SLNs showed good colloidal stability, the ability to cross an *in vitro* blood–brain barrier model, and a superior pro-apoptotic activity toward glioblastoma cells with respect to the free drug.

Conclusion—Nut-Mag-SLNs represent a promising multifunctional nanoplatform for the treatment of glioblastoma multiforme.

Keywords

blood–brain barrier; dynamic fluidic models; glioblastoma multiforme; magnetic targeting; nutlin-3a; solid lipid nanoparticles

Central nervous system (CNS) tumors are a significant cause of morbidity and mortality worldwide [1], being gliomas the most common malignant brain cancers [1,2]. Among them, glioblastoma multiforme (GBM) accounts for 50% of gliomas, and it is one of the most aggressive and incurable human cancers [3–7].

Many treatments are available for GBM, including surgical resection, chemotherapy and radiation, but despite the combination of these therapies, GBM patients can expect a median survival of just 15 months, while less than 5% of patients live longer than 5 years [3,8]. The difficulty in treating this devastating disease arises from several factors including the vast variety of genetic abnormalities that limit the use of pathway-specific targeted agents, the infiltrative nature of cancer cells that obstacles the complete surgical resection of the tumor, and the limited delivery of chemotherapeutics to brain cancer cells due to the presence of the blood–brain barrier (BBB) [9–14].

Since BBB represents one of the principal obstacles to drug delivery to tumor tissue, various strategies have been investigated to enhance brain delivery and among them, the use of nanostructures seems to be one of the most promising approaches [15–17]. Several features make nanoparticles effective in the treatment of GBM and more generally, in tumor therapy [18,19]. Being easily modifiable in terms of size, composition and surface properties, such transport systems can be properly designed to protect compounds from intracellular degradation, to avoid clearance by the immune system and to reduce toxic drug effects [3]. By exploiting passive and active targeting strategies, nanoparticles penetration through BBB can be improved, and this ability can be used to selectively deliver therapeutic compounds to the brain [17], allowing a higher cytotoxic concentration at the tumor site and a reduced toxicity in healthy cells to be achieved [20].

Many studies demonstrated both *in vitro* and *in vivo* the validity of nanocarriers for the treatment of GBM [3–16]. Poly(lactic-co-glycolic acid)or chitosan-based nanoparticles and liposomes were used to improve the efficacy of temozolomide, a systemic chemotherapeutic agent approved by US FDA for GBM treatment [9,21,22]. Preclinical studies were also performed on nanovectors in association with other drugs such as paclitaxel and doxorubicin, the anti-neoplastic activity of which was shown in a wide range of cancers, including GBM [23,24].

Although targeted delivery by nanocarriers can increase the amount of drug at the brain level, the accumulation to the tumor site can however result quite limited [25]. A solution for focusing drug-loaded nanoparticles to a specific area of the organism is offered by the exploitation of magnetically responsive nanostructures, that can be directed toward target sites through the use of magnetic fields produced, for example, by external static sources like permanent magnets [26]. In this view, the present study proposes a nanotechnological solution to increase the possibilities of treatment against GBM. The aim of this work is the development of a magnetic platform drivable through an external magnetic field, able to overcome the BBB and to selectively deliver the chemotherapy agent to the tumor cells.

The investigated drug is nutlin-3a, a potent candidate for cancer therapy that has shown its therapeutic efficacy in several cancers including GBM [27–32]. Belonging to a class of cis-imidazoline analogs, nutlin-3a represents an alternative compared with conventional chemotherapy agents, due to its ability to trigger the nongenotoxic activation of p53 tumor suppressor without inducing collateral DNA damages [32,33]. More specifically, nutlin-3a is an antagonist of murine double minute (MDM2), the primary inhibitor of p53 found to be overexpressed or amplified in several cancers, conferring tumor enhanced development, survival, chemoresistance, and poor treatment outcome [34,35]. By preventing the molecular interaction between p53 and MDM2, nutlin-3a induces the accumulation and the activation of the p53 protein, which is thus free to regulate a large number of targeted genes involved in senescence, apoptosis, cellular cycle arrest and autophagy [36]. Nutlin-3a clinical application is limited by the prohibitive doses of drug that are generally requested to obtain an adequate therapeutic concentration [37]. Nutlin-3a is, in fact, a substrate of the multidrug resistance protein MRP-1 and of the P-glycoprotein, both expressed on the luminal side of the BBB and on the membrane of tumor cells as GBM cells [38,39]. These membrane transporters are capable of pumping out from the intracellular environment the anti-tumor drugs both at the level of the BBB, thus by interfering with brain bioavailability of CNS-active molecules, and at the level of the GBM cells by protecting the tumor cells from the cytotoxic effect of the drug [15,40].

The class of nanovectors chosen in this study is represented by solid lipid nanoparticles (SLNs), the efficacy of which as drug carriers for the treatment of glioma has been already demonstrated by several works in the literature [41,42]. The SLNs are particularly appealing due to several features, among them the use of biocompatible and physiological lipids for the synthesis, the high physical stability in aqueous environments, the high drug pay load and the ability to elicit a controlled release of the incorporated drug over the span of several weeks [42,43].

Nutlin-3a and superparamagnetic iron oxide nanoparticles (SPIONs) were encapsulated in SLNs (Nutlin-loaded magnetic solid lipid nanoparticle [Nut-Mag-SLNs]) by following a solvent evaporation method. To test the Nut-Mag-SLNs ability to cross the BBB and to target tumor cells, both a static and a dynamic *in vitro* BBB model were developed. Several microfluidic BBB *in vitro* systems have been described in the literature, all of them designed with the goal to cover the existing gap between the static *in vitro* models and the complexity of an *in vivo* BBB [44–54]. We were able to improve currently available models by designing and fabricating an innovative *in vitro* dynamic system composed by two channels, an upper channel seeded with brain endothelial cells and a lower channel seeded with glioblastoma cells. Combining a commercial pump system with a software interface and a computational model, we were able to induce a constant medium flow in the upper channel mimicking the blood flow typically present in a brain capillary. To date, this is the first BBB *in vitro* model to combine the ability to recreate blood flow condition, a strong physical modelization, and the possibility to study nanovector BBB crossing ability and drug anti-cancer efficiency into a single device. Owing to this system, we were able to demonstrate the ability of Nut-Mag-SLNs to be attracted by an external magnetic field and to be internalized by endothelial cells even under dynamic flow conditions, and we further confirmed their capacity to cross BBB followed by their anti-cancer effects.

Materials & methods

SLN preparation & characterization

SLNs loaded with nutlin-3a and SPIONs were prepared through a solvent evaporation technique. A total of 10 mg of nutlin-3a (Sigma-Aldrich, MO, USA), 25 mg of cetyl palmitate (Gattefossé, Lyon, France), 25 mg of methoxyl 1,2-distearoylsn-glycero-3-phosphoethanolamine-*N*-[monomethoxy poly(ethylene glycol)] (mPEG-DSPE, 5 kD, Nanocs, NY, USA), and 3.75 mg of SPIONs (average diameter of 10 nm, EMG1300 from Ferrotec, Unterensingen, Germany) were dissolved in 500 µl of chloroform. The organic solution was then added to 2 ml of water and sonicated at 70°C for 6 min at 8000 J with a probe-tip ultrasonicator (SONOPLUS mini20, Bandelin, Berlin, Germany). Finally, the dispersion was maintained at 4°C for 30 min to stabilize the nanoparticles. Empty magnetic SLNs (Mag-SLNs) were obtained with the same procedure but without drug. To remove any solvent residuals and both nonencapsulated SPIONs and nutlin-3a, Mag-SLNs and Nut-Mag-SLNs were purified by gel chromatography using Sephadex G-25 prepacked columns (GE Healthcare Life Sciences, Little Chalfont, UK) and deionized water as eluent. To check the cellular localization of particles, fluorescein-labeled Nut-Mag-SLNs and Mag-SLNs (FITC-Nut-Mag-SLNs and FITC-Mag-SLNs) were also synthesized with the addition of 1 mg of fluorescein-PEG-DSPE (FITC-PEG-DSPE) (5 kDa, Nanocs) during the fabrication procedure. To remove FITC-PEG-DSPE in excess, fluorescent nanoparticles were centrifuged five-times at 5000 g for 10–15 min with ultrafiltration spin columns (molecular weight cutoff 300 kD, Sartorius, Goettingen, Germany).

The ζ-potential and size distribution of the samples were determined through dynamic light scattering by using a Zetasizer Nano S90 (Malvern Panalytical, Malvern, UK). All measurements were performed in triplicate. Short-term stability studies were performed by

measuring the size distribution of Nut-Mag-SLNs at 37°C in different media (water, phosphate-buffered saline solution [PBS], Dulbecco's modification of Eagle medium [DMEM] with and without 10% fetal bovine serum [FBS]) by performing multiple measurements up to 70 min. In order to assess storage and long-term stability, the measurements were repeated in the same incubation conditions at 0 and 72 h, after that Nut-Mag-SLNs have been stored at 4°C for 9 months.

The morphology and the size of the nanoparticles were analyzed by a transmission electron microscope (TEM). For this purpose, one drop of diluted Nut-Mag-SLNs was placed on a carbon-coated 200 mesh copper grids for 5 min and negatively stained with 1% uranyl acetate solution, before being allowed to dry, and the samples visualized by using a JEOL JEM-1011 microscope (JEOL Ltd, Tokyo, Japan) equipped with a tungsten thermionic gun operating at 100 kV accelerating voltage. The TEM images were acquired with an 11 MPx Orius 1000 CCD camera (Gatan, CA, USA).

The surface morphology and the shape of the formulated nanoparticles were also visualized, after gold sputtering, with scanning electron microscopy by using a FEI Helios NanoLab DualBeam microscope (Lousanne, Switzerland).

The loading of SPIONs in the SLNs was investigated by thermogravimetric analysis (TGA). Thermogravimetric analysis was performed under air at a heating rate of 10°C min^{-1} from 30 to 900°C, by using a TG/DTA 7200 Extar instrument (SII Nanotechnology Inc., Chiba, Japan).

Evaluation of encapsulation efficiency of nutlin-3a in Nut-Mag-SLNs was investigated by the reverse-phase-HPLC (RP-HPLC) method. To estimate entrapped drug in Nut-Mag-SLNs, 20 mg of freeze-dried particles were dissolved in a solution containing hexane, to solubilize the lipid matrix and to disperse SPIONs, and methanol for the extraction of nutlin-3a. After 2 h of stirring, the sample was centrifuged at 3000 rpm for 10 min (Universal 320 R, Hettich, Tuttlingen, Germany), and the methanol was analyzed for drug content by RP-HPLC with a Omnispher C18 column (250 × 4.60 mm, 110 A, Agilent Technologies, CA, USA) by using specific mobile phase for drug, at a flow rate of 1 ml min^{-1}. Nutlin-3a concentration was then estimated through calibration curve, and the obtained value was used to determinate the encapsulation efficiency by dividing the amount of drug entrapped by the total amount of drug used in the formulation, multiplied by 100; loading efficiency was also calculated by dividing the amount of drug entrapped by nanoparticles weight, multiplied by 100.

In vitro release of nutlin-3a from Nut-Mag-SLNs was carried out by placing 800 μl of Nut-Mag-SLNs (corresponding 1.2×10^{-10} M of drug) into dialysis bags (3.5 kDa, Sigma-Aldrich) immersed in a release bulk constituted by 4 ml of PBS at pH 7.4. The drug release study was carried out at 37°C in a thermostatic shaker at a rate of 150 rpm. At predetermined time points (in a range of 0–10 days), release bulk was replaced with fresh buffer solution and aliquots freeze-dried. The lyophilized products were dissolved in methanol and kept on a shaker at room temperature for 48 h. The samples were centrifuged

at 3000 rpm for 10 min to remove salts and finally the supernatants were injected in the HPLC to determine the amount of nutlin-3a.

Finally, the magnetic characterization was carried out using a superconducting quantum interference device from Quantum Design (CA, USA). Magnetization curves were measured from -50 to 50 kOe at 300 K. The temperature dependence of magnetization from 5 to 300 K after a zero-field-cooling (ZFC) and a FC was measured applying a probe field of 25 Oe.

Cell cultures & *in vitro* testing

Human glioblastoma cell line (U-87 MG) was purchased by American Type Culture Collection (VA, USA) and cultured in DMEM (Gibco, MA, USA) supplemented with 10% FBS (Gibco) and 1% penicillin–streptomycin (Gibco) at 37°C in 5% CO_2 humidified atmosphere. The effect of increasing concentrations of free nutlin-3a, Nut-Mag-SLNs, and Mag-SLNs on cell metabolic activity was investigated through WST-1 assay (Biovision, CA, USA). Cells were seeded at a density of 5×10^3 cells cm^{-2} in 24-well plates and incubated at 37°C and 5% CO_2. After overnight incubation, increasing concentrations of Mag-SLNs (0, 10, 20, 50, 100 and 200 μg ml^{-1}), Nut-Mag-SLNs (0, 10, 20, 50, 100 and 200 μg m^{-1}) and free nutlin-3a at concentrations equal to those present inside Nut-Mag-SLNs (0, 0.12, 0.25, 0.66, 1.33 and 2.66 μM) were tested, while cells incubated with medium only were used as a control. Cell metabolic activity was assessed after 24 and 72 h since the beginning of the treatment following the WST-1 protocol: 300 μl of culture medium + 30 μl of the premix solution were added to each well and incubated for 1 h. The absorbance of the supernatants was finally read at 450 nm with a microplate reader (Victor3, Perkin Elmer, MA, USA).

Uptake of Nut-Mag-SLNs by U-87 MG cells was studied by using confocal microscopy. Cells were seeded at a density of 17×10^3 cell cm^{-2} in Ibidi μ-Dishes (35 mm, Ibidi, Martinsried, Germany), incubated overnight at 37°C and treated with FITC-Nut-Mag-SLNs at a concentration of 100 μg ml^{-1}. After 24 h of treatment, cells were rinsed with PBS, fixed in 0.25% paraformaldehyde (PFA, Sigma-Aldrich), treated with Triton 0.1% X-100 and blocked for 1 h with a goat serum solution (10% in PBS). Finally, cells were incubated with a staining solution containing TRITC-phalloidin (1:100, Sigma-Aldrich) and Hoechst 33342 (1:1000, Invitrogen, MA, USA) to label f-actin and nuclei, respectively. A confocal microscope (C2s, Nikon, Tokyo, Japan) was used for the acquisition of the images.

Prussian Blue iron staining was instead performed to detect the presence of SPIONs in U-87 MG cells, previously treated with Nut-Mag-SLNs. The U-87 MG cells were seeded at a density of 10×10^3 cell cm^{-2} in 24-well plates and incubated overnight at 37°C, before being treated with 100 μg ml^{-1} of Nut-Mag-SLNs. After 24 h of incubation, cells were washed with PBS, fixed in 0.25 % PFA (Sigma-Aldrich) for 8 min at 4°C, permeabilized with 100% methanol at -20°C for 10 min, rinsed with distilled water and incubated for 30 min in a solution obtained by mixing equal parts of 20% hydrochloric acid and 10% potassium ferrocyanide trihydrate (all from Sigma-Aldrich). Nuclei were counterstained with nuclear fast red (Fluka, Bucharest, Romania) for 10 min. After three washes with water, cells were observed with an inverted microscope (TE2000U, Nikon), equipped with a cooled CCD camera (DS-5MC USB2, Nikon) and with NIS Elements imaging software for image acquisition.

For the study of the intracellular localization of Nut-Mag-SLNs, U-87 MG and bEnd.3 cells seeded on Ibidi μ-Dishes were pre-treated with FITC-Nut-Mag-SLNs for 72 h and subsequently washed twice and stained with Lysotracker (75 nM, Invitrogen) and Hoechst 33342 (1 μg ml^{-1}, Invitrogen) in serum-free DMEM at 37°C for 30 min. Cells were then fixed for 20 min at 4°C in 4% PFA, stained with Alexa Fluor 647 phalloidin (100 μM, Millipore, Burlington, MA, USA) at 37°C for 1 h, washed twice in PBS and then analyzed through confocal microscopy (C2s, Nikon).

To investigate apoptosis phenomena, U-87 MG cells were seeded at a density of 5×10^3 cells cm^{-2} in six-well plates and maintained at 37°C. After overnight incubation, cells underwent a treatment with 100 μg ml^{-1} of Nut-Mag-SLNs, 100 μg ml^{-1} of Mag-SLNs, 1.33 μM of nutlin-3a and with fresh medium. After an incubation period of 72 h, cells were collected by centrifugation at 2500 rpm for 7 min, washed twice with PBS and finally resuspended in 300 μl of PBS containing 2.5 μM of annexin V-FITC (Thermo Fisher, MA, USA) and 1 μg ml^{-1} propidium iodide (Sigma-Aldrich) for 10 min at 37°C in the dark. Apoptotic cells were determined by analyzing 60,000 ungated cells by using a flow cytometer (Coulter Cytoflex, Beckman, CA, USA) and the FlowJo software.

To investigate the effect of nutlin-3a and of Nut-Mag-SLNs on the expression of p53 and its downstream proteins (e.g., MDM2 and p21), western blotting analysis was performed. In particular, U-87 MG cells were seeded at a density of 5×10^3 cells cm^{-2} in T-75 flasks, incubated overnight at 37°C and treated with 100 μg ml^{-1} of Nut-Mag-SLNs, 100 μg ml^{-1} of Mag-SLNs, 1.33 μM of nutlin-3a and with the plain medium as a control. After 72 h of treatment, cells were centrifuged at 2500 rpm for 7 min, washed with PBS and finally obtained pellets were incubated with RIPA lysis buffer (Sigma-Aldrich) containing serine/threonine and tyrosine phosphatase inhibitors and a protease inhibitor cocktail 1× (S8830, Sigma-Aldrich). Samples were then homogenized by using three 10 s pulses applied with probe-tip ultrasonicator (SONOPLUS mini20, Bandelin) set at 8000 J in an ice bath. Lysates were centrifuged at 9000 rpm for 30 min at 4°C, and protein concentration in supernatants was determined by the BCA protein assay (Thermo Scientific). Proteins (20 μg $lane^{-1}$) were then separated on a 4–15% polyacrylamide gel (Bio-Rad, CA, USA) under reducing conditions and transferred to a nitrocellulose membrane (Trans Turbo Blot system, Bio-Rad). To detect p21 protein, the membrane was blocked with 5% dry fat milk in 0.1% Tween/Tris Buffer Saline (T-TBS) for 1 h at room temperature and then incubated overnight at 4°C with rabbit monoclonal anti-p21 antibody (1:4000 in T-TBS, EPR362, Abcam, Cambridge, UK). To evaluate p53 and MDM2 proteins, the blot membranes were blocked with 3% bovine serum albumin (BSA, Sigma-Aldrich) in T-TBS for 1 h at room temperature and then incubated overnight at 4°C either with mouse monoclonal anti-p53 antibody (1:4000 in 1% BSA/T-TBS, PAb 1801, Abcam) or with mouse monoclonal mouse anti-MDM2 antibody (1:20000 in 1% BSA/T-TBS, SMP 14, Abcam). Mouse monoclonal anti-β-actin antibody (1:5000 in T-TBS, Sigma-Aldrich) was used as protein loading control on blot membrane previously incubated with 5% dry fat milk in T-TBS for 1 h.

Anti-rabbit and anti-mouse HRP-conjugated antibodies (1:3000 in 5% milk/T-TBS, Bio-Rad) were used as secondary antibodies and immunocomplexes were detected by chemiluminescence (ECL clarity, Bio-Rad), by using Chemi-Doc XRS+ system (Bio-Rad).

All reactions were performed at room temperature unless otherwise specified. Image Lab software (Bio-Rad) was used to evaluate the molecular weights and the density of the resulting bands.

To investigate the subcellular localization of p53, p21 and MDM2 proteins after treatment with nutlin-3a and Nut-Mag-SLNs, immunofluorescence was performed. The U-87 MG cells were seeded at a density of 5×10^3 cells cm^{-2} on glass coverslips and incubated at 37°C overnight. Following day, cells were incubated with medium containing 100 μg ml^{-1} of Nut-Mag-SLNs, 100 μg ml^{-1} of Mag-SLNs or 1.33 μM of nutlin-3a. Cells treated with the plain medium were used as a control. After 72 h of treatment, cells were fixed in 0.25% PFA (Sigma-Aldrich) for 8 min at 4°C, permeabilized with Triton 0.1% X-100 (Sigma-Aldrich) for 15 min and blocked with 10% goat serum solution for 1 h. Cells undergone different treatments were incubated overnight at 4°C with 10% goat serum solution containing monoclonal anti-p53 antibody (1:200, PAb 1801, Abcam), mouse monoclonal mouse anti-MDM2 antibody (1.200, SMP 14, Abcam) or rabbit monoclonal anti-p21 antibody (1:400 EPR362, Abcam). Samples were washed three-times in PBS and incubated either with Atto 488 goat anti-rabbit secondary antibody (1:200, Sigma-Aldrich) or with Alexa Fluor 488 goat anti-mouse secondary antibody (1:200, Millipore) in 10% goat serum at 37°C for 45 min. Nuclei were counterstained with Hoechst 33342 (1:1000, Invitrogen) and f-actin with TRICT-phalloidin (1:100, Sigma-Aldrich). After three PBS rinsing, images were acquired by a confocal microscope (C2s, Nikon). Quantitative evaluation was performed by counting p53/MDM2/p21 positive cells over the total number of cells.

Static *in vitro* blood–brain barrier model

The bEnd.3 cells (Sigma-Aldrich) were used in order to establish a BBB *in vitro* model and were grown in DMEM supplemented with 10% FBS, 1% penicillin-streptomycin, 1% nonessential amino acids (NEAA) and 5 μM 2-mercaptoethanol at 37°C in 5% CO2 humidified atmosphere (all reagents from Gibco). For all experiments, cells were trypsinized and seeded at a density of 36×10^3 cell cm^{-2} onto transwell permeable supports (400 nm pores size polyester membranes, Sigma-Aldrich) precoated with gelatin 1%. Cells were incubated at 37°C with 5% CO_2 for 5 days to form a monolayer of endothelial cells on the filter. To induce the tight junctions protein expression between adjacent endothelial cells, 24 h before starting all studies, the medium of apical and basal chamber was supplemented with 8-(4 chlorophenylthio)adenosine 3′,5′ cyclic monophosphate sodium salt (pCPT-cAMP) 250 μM (Sigma-Aldrich), 4-(3-butoxy-4-methoxybenzyl) imidazolidine-2-one (Sigma-Aldrich) 17.5 μM (Sigma-Aldrich) and hydrocortisone 550 nM (Sigma-Aldrich).

To assess the restrictiveness and the integrity of the bEnd.3 cell monolayer, the bioelectric properties and the permeability to solutes were investigated after 5 days since seeding. Apical and basal chambers of transwell inserts were filled with DMEM without serum and phenol-red for 30 min. After this period of incubation, transendothelial electrical resistance was measured with Millicell ERS-2 (Electrical Resistance System, Millipore).

For permeability studies, the diffusion of 4 kD FITC-dextran (Sigma-Aldrich), 70 kD FITC-dextran (Sigma-Aldrich) and 66 kD FITC-BSA (FITC-BSA, Sigma-Aldrich) from the apical to the basolateral direction across the bEnd.3 monolayer was investigated. For all analyzed

tracers, 50 μl of the fluorescent solution was added to the apical chamber to obtain a final concentration of 2 mg ml-1 in a volume of 300 μl. Cells were incubated at 37°C and after 3 h, 100 μl samples of medium were taken from the basolateral chambers to measure the fluorescence into 96-well black plates through a microplate reader (Victor3, PerkinElmer; excitation 485 nm, emission 544 nm). Each measure was performed in triplicate, and the diffusion of the fluorescent molecules through the BBB model was compared with diffusion across empty filters precoated with gelatin 1%.

As a further characterization, bEnd.3 cells on the fifth day of culture at confluence on porous transwell filters were investigated for ZO-1 expression. After fixation with 4% PFA for 20 min at 4°C and permeabilization with Triton 0.1% X-100 for 15 min, cells were blocked with 10% goat serum solution for 1 h and incubated with primary antibody ZO-1 (2.5 μg ml^{-1}, Invitrogen, CA, USA) for 3 h at room temperature with 10% goat serum. Cells were washed three-times in PBS and incubated with staining solution containing Atto 488 goat anti-rabbit secondary antibody (1:200, Sigma-Aldrich), TRITC-phalloidin (1:100, Sigma-Aldrich) and Hoechst 33342 (1:1000, Invitrogen) at 37°C for 45 min. After three PBS rinsing, images were acquired by confocal microscope (C2s, Nikon).

BBB crossing investigation

To test Nut-Mag-SLNs ability to selectively deliver the drug to U-87 MG cells across the BBB model, viability assay was performed both on the BBB model and on U-87 MG cells. Once verified that the bEnd.3 cell monolayer shows strong barrier properties, transwell inserts containing the BBB model (previously described) were transferred into 12-well plates where U-87 MG cells were seeded the previous day at a density of 5×10^3 cell cm^{-2} and incubated overnight at 37°C. Total 400 μl of medium containing 600 μg ml^{-1} Nut-Mag-SLNs or 600 μg ml^{-1} Mag-SLNs were added to the apical side of the BBB layers, while BBB layers treated with plain medium were used as a control. To each basolateral well, containing the U-87 MG cells, 1200 μl of fresh medium were added. After 72 h of treatment, WST-1 metabolic activity assay (Biovision) was performed. Both U-87 MG cells and BBB layers were incubated with the WST-1 reagent (previously 1:10 diluted with culture medium) for 1 h at 37°C and, finally, the absorbance was read at 450 nm with a microplate reader (Victor3, Perkin Elmer).

Immunostaining of the BBB model was also carried out to evaluate the endothelial layer integrity after the nanoparticle crossing. After 72 h of incubation, BBB layers were fixed in 4% of PFA for 20 min at 4°C, blocked with 10% goat serum for 1 h and incubated for 3 h at room temperature with primary antibody ZO-1 (2.5 μg ml^{-1}, Invitrogen) diluted in 10% goat serum solution. After extensive washes in PBS, staining solution with Atto 488 goat anti-rabbit secondary antibody (1:200, Sigma-Aldrich) and Hoechst 33342 (1:1000, Invitrogen) was added and incubation carried out at 37°C for 45 min. Images were acquired by confocal microscope (C2s, Nikon) after three washes in PBS.

Finally, flow cytometry evaluation of nanoparticles (fluorescently labeled) crossing was also performed. After 72 h of incubation, both BBB layers and U-87 MG cells were collected by centrifuge, resuspended in 300 μl of PBS, and analyzed by flow cytometer (Coulter Cytoflex, Beckman) and the FlowJo software.

Europe PMC Funders Author Manuscripts

Dynamic experiments

The BBB dynamic *in vitro* system was fabricated combining laser cutting technology and thermal ethanol bonding of poly(methyl methacrylate) (PMMA) sheets [50]. The PMMA sheets were cut using a laser cutting machine (Universal Laser Systems, Wien, Austria) with a source power of 50 W and a laser spot of 100 μm^2.

The final device was composed of several square (5 × 5 cm^2) optically clear layers of PMMA: a bottom layer (175 μm thickness), a second layer (500 μm thickness) hosting the lower channel of the system, a third layer (175 μm thickness) acting as a support for a porous membrane (Polyester Corning insert, 10 μm thickness, 400 nm pores size), a fourth layer (500 μm thickness) hosting the upper channel and lastly a top layer (5 mm thickness) acting both as a cap and as a reservoir for cell culture media (see Supplementary Figure 1 for details). Both channels were cut to have 5 mm width. The layers were bonded together by adding 100 μl of ethanol (96.0–97.2% Sigma-Aldrich) between each sheet, and then by applying a pressure through the use of screw clamps for 5 min at 70°C. After the assembly, the devices were washed two times with water and sterilized with ethanol.

After coating with gelatin 1%, bEnd.3 cells were seeded on the porous support separating the two chambers, while U-87 MG cells were seeded in the lower chamber (cell density 6 × 10^4 cm^{-2}) with high glucose medium supplemented with 10% FBS and 1% penicillin/streptavidin. After 5 days since the seeding, permeability test using FITC-dextran 4 kDa was performed as previously described, in order to confirm the formation of a tight endothelial cell layer between the two chambers.

Dynamic studies were performed using an Ibidi pump system and a software interface developed by our group. Cell culture medium was pumped in the upper channel with a flow rate of 12 ml min^{-1}. The flow rate value was defined based on a theoretical model of the flow field in the channel cross-section (see Supplementary Information), in order to enforce on brain endothelial cells a shear stress around 12 dyn cm^{-2} (i.e., 1 Pa, see Supplementary Figure 2), as typical in capillaries [55]. The medium flow direction was inverted every 15 s through the use of an electric valve.

To study the possibility to attract Nut-Mag-SLNs through an external magnetic source, 50 μg ml^{-1} of both Mag-SLNs and Nut-Mag-SLNs were injected into the system, and a cylindrical permanent magnet (13 mm diameter, 10 mm width, grade N35 NdFeB, axial magnetization) was placed in contact with the bottom PMMA layer, with the axis passing through the center of the channel top view (see Supplementary Figure 1). After 30 min of dynamic experiment, the medium flow was stopped and the cultures were imaged through confocal microscopy to analyze the particle spatial distribution. After the acquisition of the confocal images, the cultures were left in incubation at 37°C in static condition without any magnetic field, and effects of nanoparticles on U87-MG cell seeded in the lower chamber of the system were evaluated after 72 h, both with WST-1 and with the Live/Dead (Thermo Fisher) assays. The WST-1 test was performed as previously described, while the Live/Dead assay was carried out by staining cultures in PBS supplemented with 1 μM of calcein-AM and 1 μM of ethidium homodimer-1 for 20 min at 37°C. Stained cells were then analyzed through a fluorescence microscope (Nikon Eclipse Ti).

Europe PMC Funders Author Manuscripts

A computational model was introduced for predicting the distribution of Nut-Mag-SLNs on the porous membrane under dynamic flow conditions. We leveraged analytical expressions for both the fluid field (see Supplementary Information) and the magnetic field, and we adopted a point-dipole approximation for the force induced by the external permanent magnet on the magnetoresponsive carriers [56]. Using the Matlab environment, we numerically integrated the trajectories of nearly 1.25 million carriers, thus deriving the sought distribution on the membrane. Relevant details are reported in Supplementary Information.

Statistical analysis

Statistical analysis was performed using R software. The normal distribution of dataset was analyzed through Shapiro–Wilkinson test. For normally distributed data, we used one-way ANOVA followed by Bonferroni's *post hoc* correction or the two-tailed unpaired t-test. For non-normally distributed data, we used Kruskal–Wallis test followed by pairwise-Wilcoxon *post hoc* correction. Non-normal data distributions were expressed as median ±95% CI and were shown in boxplots. Statistical significance was set at a $p < 0.05$.

Results

Physicochemical characterization of Nut-Mag-SLNs

In order to obtain a drug-delivery system for nutlin-3a, drug-loaded cetyl palmitate/mPEG-DSPE SLNs were synthesized by a solvent evaporation technique. Obtained nanoparticles present a spherical shape, as demonstrated by both TEM and scanning electron microscopy (Figure 1A) imaging. From TEM imaging, in particular, it is possible to appreciate the presence of the SPIONs (electron-dense darker spots) in the lipid matrix.

In water, Nut-Mag-SLNs present an average size of 180 ± 40 nm and a ζ-potential of -40.0 ± 1.4 mV. Despite the absence of surfactants during the preparation, nanoparticles present optimal colloidal stability without evidence of aggregation, as shown by the short-term stability studies performed for over 1 h at 37°C in different media (water, PBS, DMEM with and without 10% FBS, Figure 1B). The measurements were then repeated after a long-term storage of Nut-Mag-SLNs (9 months at 4°C); these nanoparticles have been incubated in different media as previously described up to 72 h, and results (showed again in Figure 1 B) demonstrate that even after 9 months of storage they maintain an excellent colloidal stability.

From the comparison of the thermal degradation behaviors under air flow, a SPION loading of about 10 wt% could be estimated (Figure 1C). Finally, RP-HPLC revealed a drug-loaded amount of 160 μg for 20 mg of Nut-Mag-SLNs, showing a encapsulation efficiency of about 2% and a loading efficiency of 0.8%.

The *in vitro* release study of the drug from Nut-Mag-SLNs is shown in Figure 1D. Nut-Mag-SLNs exhibit an initial rapid release, during which drug release reached 26 ± 2.3% and 47 ± 5.2% after 1 and 3 days, respectively. During following period, the release was continuous but slower, by reaching 72.0 ± 0.3% after 10 days.

Figure 2A represents the magnetic field dependence of the magnetization of bare SPIONs and of Nut-Mag-SNLs measured at room temperature. The two curves exhibit a similar shape, and there are no coercivity or remanence, as can be observed also in Figure 2B, being the main difference in their respective specific magnetizations. In fact, the specific saturation magnetization measured with a magnetic field of 50 kOe of the bare SPIONs is 56.1 emu g^{-1}, while in the Nut-Mag-SLNs it is 1.73 emu g^{-1}. The magnetic behavior was further investigated by measuring the temperature dependence of the magnetization in the ZFC and in the FC conditions (Figure 2C). The ZFC curve of the bare SPIONs exhibits a broad maximum centered around 175 K. The FC magnetization is almost constant (increases slightly) from low temperature to 175 K, the temperature at which the FC curve joints the ZFC curve. The ZFC curve of the Nut-Mag-SNLs exhibits a narrower peak with a maximum at 150 K that corresponds to the average blocking temperature. The magnetization of the FC curve decreases continuously from low temperature joining to the ZFC curve above 175 K. These features indicate that the bare SPIONs are much more magnetically correlated, forming aggregates, with respect to their conditions inside the Nut-Mag-SLNs [57]: this suggests that after the Nut-Mag-SNLs preparation, SPIONs are better dispersed in the lipid matrix with respect to the ‘bare’ condition. On the other hand, the ZFC and FC magnetization curves of the two samples overlap at the same temperature around 175 K. This indicates that the nanoparticles exhibit a superparamagnetic behavior above 175 K. Above this temperature, the magnetization can overcome the effective magnetic barrier correlated to the magnetic anisotropy due to the dominant role of the thermal activation demagnetization processes [58]. In such case, no hysteresis should be observed as experimentally observed in Figure 2B in both samples.

In vitro cytotoxicity study & internalization

Biological effects of increasing concentrations of Nut-Mag-SLNs, Mag-SLNs and free nutlin-3a after 24 and 72 h of incubation were investigated through WST-1 metabolic activity assay, by using U-87 MG cell line as a glioblastoma model system. As shown in Figure 3, Mag-SLNs revealed high biocompatibility at both time points examined with no impairment of cell metabolism. The anti-neoplastic effect of the free drug was appreciable after 24 h of treatment at the highest tested concentration only, by obtaining a viability reduction of about 10% (Figure 3A). After 72 h of incubation, free nutlin-3a concentrations of 0.25 and 0.66 μM caused a reduction of cell metabolic activity of about 10%, which however was not statistically significant; this effect resulted increased at the highest drug concentrations (1.33 and 2.66 μM), by obtaining 20% of metabolic activity reduction (Figure 3B). With respect to the plain drug, Nut-Mag-SLNs exhibited a higher cytotoxic effect, already after 24 h of treatment, further enhanced at 72 h of incubation (Figure 3A & B). After 3 days of treatment, Nut-Mag-SLNs increased the amount of drug delivered to the cells, leading to a reduction of the metabolism from 80 to 50%, by using 0.12–2.66 μM of encapsulated drug. Altogether, these data show a good biocompatibility of the plain Mag-SLNs, and an enhanced effect of the drug when loaded in the Nut-Mag-SLNs.

Cellular uptake was investigated by confocal microscopy, and Figure 4A clearly shows a strong accumulation of FITC-Nut-Mag-SLNs by cancer cells in the perinuclear position after 24 h of incubation (f-actin in red, nuclei in blue, nanoparticles in green). The

intracellular localization of the particles was further investigated by using the Lysotracker dye. As shown in Supplementary Figure 3, bEnd.3 showed just a partial internalization of nanoparticles in correspondence of the acidic compartments ($r = 0.47$), while for U-87 MG cells the colocalization of FITC-Nut-Mag-SLNs with the Lysotracker signal is almost complete ($r = 0.91$).

The SPION presence in the cells upon Nut-Mag-SLN internalization uptake by U-87 MG cells was qualitatively confirmed by Prussian blue staining, a method which allows identifying intracellular iron through the formation of blue precipitates. After 24 h of incubation with Nut-Mag-SLNs, U-87 MG cells were stained with Prussian blue and blue-stained iron nanoparticles were clearly visible in perinuclear position (Figure 4B, on the left). In the control samples, no blue precipitates could be appreciated (Figure 4B, on the right).

Apoptosis phenomena investigation

The ability Nut-Mag-SLNs to induce apoptosis in U-87 MG was compared with that of the plain drug using flow cytometry. Apoptosis is a form of cell death and its deregulation is associated with several cancers, thus restoring normal apoptosis in tumor cells is one of the main targets of cancer therapy [59]. Quantitative evaluation of nutlin-3a mediated apoptosis was performed by annexin V-FITC/propidium iodide assay, a staining procedure that allows discriminating live, apoptotic, or necrotic cells. We found that Nut-Mag-SLNs are much more effective with respect to the plain drug in inducing cell death (Figure 5). At same nutlin-3a concentration (1.33 μM), Nut-Mag-SLNs led in fact to a significant increase of total death cells (75.1%) with respect to the plain drug (45.8%). More precisely, after 72 h of treatment with plain drug, results indicated 28.4% of late apoptotic, 7.0% of early apoptotic, and 10.4% of necrotic cells. A higher population of late apoptotic (47.1%) and necrotic cells (23.7%) were instead observed following the treatment with Nut-Mag-SLNs, where early apoptotic cells represented the 4.3% of the population. Finally, samples untreated or treated with empty Mag-SLNs showed analogous percentages of live, apoptotic, and necrotic cells. Coherently with metabolic data, apoptosis investigation confirmed the high biocompatibility of used drug-delivery system, as well as the increased chemotherapeutic activity of Nut-Mag-SLNs with respect to same concentrations of free drug (quantitative analysis of the annexin V-FITC/propidium iodide assay is summarized in Supplementary Figure 4).

To clarify the molecular mechanism by which nutlin-3a (both free and delivered by the nanoparticles) induces anti-proliferative effects, p53, p21 and MDM2 protein expression was analyzed through western blotting (Figure 6A; full-length blots are provided in Supplementary Figure 5). Many works in the literature in fact report that augmented expression of such proteins is correlated to the cytotoxic effect of the drug [28–30]. Our results demonstrate that after 72 h of incubation, Mag-SLNs did not induce any increments in the expression for all the investigated proteins with respect to the control (cells treated with plain medium), therefore demonstrating the inability of used carriers to activate anti-neoplastic effects through studied proteins and thus confirming their inherent biocompatibility. Concerning treatment with the free drug, no evidences of significant expression increment were detected for p53 and MDM2 proteins, while p21 expression

resulted twofold increased with respect to the control. By contrast, induction of p53, p21 and MDM2 became much more evident following the incubation with Nut-Mag-SLNs delivering the same amount of drug. In particular, with respect to control cultures and to cells treated either with empty nanoparticles or with the plain drug, p53 and p21 expression levels resulted significantly higher (almost threefold for p53 and ninefold for p21, Figure 6B). Concerning MDM2, despite protein levels seem to increase after the incubation with Nut-Mag-SLNs, the detected difference was not significantly different with respect to the other treatments.

The intracellular localization of p53, MDM2 and p21 was moreover investigated by immunofluorescence (Figure 7A). Results show that, in control cells and in cultures treated with empty Mag-SLNs, p53 and MDM2 were diffusely distributed in the cytoplasm. However, their localization patterns changed after the incubation with free drug and Nut-Mag-SLNs, showing strong nuclear accumulation of both p53 and MDM2. The quantitative analysis, reported in Figure 7B, illustrates that the percentage of cells with nuclear localization of p53 and MDM2 (81.1 ± 1.5% and 80.6 ± 5.1% respectively) after the treatment with Nut-Mag-SLNs was significantly higher with respect to that one of cultures treated with the same amount of plain drug (46.7 ± 5.2% and 39.3 ± 6.1% for p53 and MDM2, respectively). Concerning p21, this protein showed a nuclear accumulation already in control and Mag-SLNs-treated cultures; however, this phenomenon resulted significantly enhanced after the treatment with the plain drug (77.2 ± 1.7%), reaching 98.0 ± 3.5% following incubation with Nut-Mag-SLNs.

Characterization of the blood–brain barrier model

To obtain an *in vitro* BBB model, bEnd.3 cells were seeded on a polyester membrane, able to sustain cell attachment and growth, and that separates an upper and a lower compartment of 24-well culture plates. The cells were also exposed to cAMP and hydrocortisone to induce the formation of tight junctions among endothelial cells [60] and, after 5 days from seeding, the transendothelial electrical resistance value was 40 $\Omega \cdot cm^2$.

The permeability to dextran of different molecular weights and to BSA was investigated, and results are reported in Supplementary Figure 6A. Fluorescently labeled dextran was used as tracer of the paracellular permeability [61], and data show that the diffusion of the 4 kD FITC-dextran across the *in vitro* BBB model was 50% reduced with respect to the plain membranes (without endothelial cell cultures, considered as control), while only the 14% of 70 kD FITC-dextran reached the bottom of the transwell, again with respect to the control. These results thus confirm the formation of an *in vitro* BBB model capable to restrict the paracellular diffusion in a size-selective manner. Through the study of the FITC-BSA, diffusion was instead analyzed along the transcellular pathway [62], demonstrating that bEnd.3 monolayer prevented the passage of the solutes also by such route: in fact, only 33% of FITC-BSA could cross the BBB model with respect to the control.

Finally, the formation of the tight endothelial monolayer was confirmed by immunofluorescence, which showed strong membrane localization of ZO-1 (in green, Supplementary Figure 6B). The study of this protein is a good indicator to evaluate *in vitro* barrier models [63], being a marker of tight junctions, which are contact sites among

adjacent endothelial cells that act as a semipermeable barrier (or gate) to the paracellular transport of ions, solutes, water and various macromolecules [11]. From Supplementary Figure 6B, we can appreciate the compactness of the cell layer (no significant extracellular spaces being featured therein), which contributes to hinder the passage of molecules between the two model compartments.

BBB crossing & Nut-Mag-SLN effects

To evaluate tumor cell targeting and delivery efficiency of Nut-Mag-SLNs across the BBB model, metabolic activity assay was performed on U-87 MG cells and on bEnd.3 layers. Following the incubation with magnetic nanoparticles (both empty, as a control, and loaded with the drug) no evidence of cytotoxicity was detected at the tested concentration (600 μg ml^{-1}) on the bEnd.3 layer, being the metabolic activity of the cells not affected by the treatment with the nanoparticles (Figure 8A). Concerning U-87 MG cells, good cytocompatibility of the empty Mag-SLNs was confirmed upon BBB crossing (no alteration in cell metabolic activity was indeed observed); conversely, Nut-Mag-SLNs induced an anti-proliferative effect against tumor cells leading to a reduction of viability to 50% (Figure 8A) upon BBB crossing. These data demonstrate that Nut-Mag-SLNs are able to act on cancer cells following the BBB model crossing, efficiently delivering the drug to U-87 MG cells without affecting endothelial cells viability.

To better understand whether nanoparticles passage affects BBB model integrity leading to alteration of tight junctions, qualitative evaluation of ZO-1 expression was investigated by immunostaining, and no significant alteration in the ZO-1 pattern was highlighted before and after the nanoparticle treatment, just suggesting no harmful effects during the BBB model crossing (Supplementary Figure 7A).

The Nut-Mag-SLNs ability to be internalized by endothelial cells and to reach cancer cells was further confirmed by flow cytometry analysis (Figure 8B and Supplementary Figure 7B); in particular, bEnd.3 cells showed a statistically significant increment of fluorescence due to internalization of FITC-stained nanoparticles at each analyzed time points analyzed, while U-87 MG seeded on the basolateral side of the transwell inserts showed statistically significant higher values of fluorescence just after 72 h of treatment with the fluorescent-labeled nanoparticles.

Dynamic targeting testing

An *in vitro* dynamic BBB model was developed for the final assessment of the magnetically driven drug targeting (Supplementary Figure 1): the device was exploited to demonstrate that Nut-Mag-SLNs can be actively guided so as to foster their passage across BBB, by means of an external magnetic field. The possibility to obtain an endothelial cell layer on the porous membrane separating the two chambers of the system with good ‘barrier properties’ was confirmed by measuring the diffusion of 4 kD FITC-dextran as previously described for the static assays (Supplementary Figure 8).

As shown in Figure 9, in the presence of a magnet positioned under the system more Nut-Mag-SLNs tend to be internalized by endothelial cells and to reach U87-MG compared with experiments carried out in absence of the magnet. More in details, the distribution of

nanoparticles attracted by the external magnet onto the porous membrane is depicted in Figure 10. The reported images show a bright field acquisition (first row), a fluorescence acquisition (second row, acquired by using FITC-Nut-SLNs) and a merging (third row) demonstrating a peculiar accumulation of the magnetic nanovectors in correspondence of the magnet edge. The observed distribution was remarkably predicted by the numerical model (fourth raw). Indeed, besides describing relevant contributions to carrier capture due to viscous effects close to the channel boundaries, the model clearly highlighted the strong attractive actions induced by the magnet near its top edge (minor deviations with respect to the microscope acquisitions being likely induced by sample manipulation). This result further underlines the value brought by theoretical/computational approaches to the design/development of *in vitro* dynamic BBB models.

The Nut-Mag-SLNs confirmed their anti-cancer activity as shown by the fluorescent images of Figure 11A, that highlight an increment of the levels of cellular death with respect to an analogous treatment with plain Mag-SLNs (in both cases the particles were attracted using a magnet). In particular, U87-MG cells magnetically targeted with Mag-SLNs showed a dead/live cells area ratio of about 4%, while the accumulation of Nut-Mag-SLNs caused an increment of dead/live cells area ratio to about 25% ($p < 0.05$; Figure 11B). Magnetically guided Nut-Mag-SLNs were also able to cause a reduction in the U87-MG metabolic activity of about 40% with respect to plain Mag-SLNs (Figure 11C).

Discussion

The GBM is the most aggressive brain tumor with a highly malignant course and a poor treatment response. Although many efforts have been made to develop diagnostic and therapeutic tools, the treatment of GBM remains a massive challenge in neuro-oncology, and successful treatments are still far from being attained [3].

In this framework, the present work proposes a nanotechnology-based solution by targeting cancer cells with nutlin-3a-loaded magnetic nanovectors. Despite nutlin-3a anti-tumor activity has been shown on several types of cancers [27–30], a few works in the literature reported its encapsulation in nanoparticulate drug delivery systems to improve therapeutic efficacy [37,38,64,65], and no studies concerning its association with magnetic nanoparticles can be found: for the first time, magnetic SLNs loaded with nutlin-3a have been prepared, characterized, and *in vitro* tested, demonstrating to be a promising multifunctional tool against glioblastoma.

Cetyl palmitate and mPEG-DSPE were selected as main components of the nanovectors, and from obtained results, it is possible to conclude that they are suitable materials to produce highly biocompatible nanoparticles with excellent colloidal stability. Both mPEG-DSPE and cetyl palmitate allow to obtain amphiphilic nanoparticles without the use of surfactants, thus constituted by hydrophilic moieties on their surface that ensure dispersibility and stability in biological media, and by a solid lipid core comprising the hydrophobic tails of the mPEG-DSPE embedded in a cetyl palmitate matrix. The lipid nature of the nanoparticles allows the interaction with the hydrophobic drug, which is loaded and stably incorporated in the lipid core. Moreover, it was reported that PEG reduces adsorption of proteins from bloodstream to

the nanoparticles surface, thus limiting the uptake by the reticuloendothelial system and increasing circulation time [66]. Through adopted synthesis method, we developed nanoparticles with size and negative surface charge appropriate for brain delivery [67] and that present a satisfactory stability in physiological conditions.

The biological activity of Nut-Mag-SLNs was tested on U-87 MG glioblastoma cell line, and our results clearly demonstrate that Mag-SLNs represent an optimal drug-delivery system for nutlin-3a. Our nanoplatform exerts a higher anti-tumor activity with respect to the plain drug, allowing achieving 50% reduction in metabolic activity with a significantly lower amount of drug. This result can be attributed to an enhanced Nut-Mag-SLNs ability to penetrate the tumor cells when compared with the free drug. Many previous works demonstrated that the use of nanoparticle carriers, such as SLNs, is a valid strategy for improving drug delivery to cells [68]. Nanoparticles are in fact able to bypass drug efflux pumps expressed on human cancer cells, thus increasing intracellular drug concentration [69]. Our particles showed to be highly internalized by cancer cells in correspondence of acidic subcellular compartment, and as widely described in the literature the exposure of lipid nanoparticles to an acidic environment could lead to a disruption of the lipid matrix with a consequent release of compounds encapsulated within [70].

Nutlin-3a is well known for inducing apoptosis in many cancer cells, the primary mechanism of tumor growth inhibition that leads to cell death [59]. Nut-Mag-SLNs resulted in being much more effective with respect to the free drug in activating the apoptotic response, leading to a substantial increment of cell death. These results were validated by the analysis of the expression of proteins implicated in drug action mechanism, such as MDM2, p53 and p21 [28–30]. As previously mentioned, in tumors where MDM2 is overexpressed and p53 is wild type, use of p53-MDM2 interaction inhibitors like nutlin-3a represents a valid therapeutic strategy, so that p53 can trigger processes of apoptosis, senescence and cellular cycle arrest [33]. From our results, it is evident that nutlin-3a encapsulation in Mag-SLNs improves the potential of the drug in restoring p53 pathway, thus leading to a greater apoptotic effect. Due to higher uptake of Nut-Mag-SLNs, augmented intracellular drug accumulation efficiently prevents the molecular interaction between p53 and MDM2 with respect to the plain drug, by inducing the stabilization and the accumulation of p53, which is thus free to promote the expression of downstream proteins. An indication of augmented p53 activity following treatment with Nut-Mag-SLNs was the significant increase in p53 and p21 protein levels. It is known that augmented expression of such proteins is a direct consequence of nutlin-3a-mediated p53 transcriptional activity [28,36,71]; therefore, the higher apoptotic effect of Nut-Mag-SLNs is strictly associated with a high expression of the investigated proteins [38,71]. Concerning MDM2, this protein is transcriptionally inducible by p53, and in our work the expression levels increased after the incubation with Nut-Mag-SLNs [71]. The detected difference was not significant with respect to the other treatments, and such result can be attributed to high basal MDM2 levels in U-87 MG cells [72]; this cell line, in fact, is an optimal glioblastoma tumor model to test drugs like nutlin-3a, due to MDM2 overexpression and for p53 wild-type, which are two essential conditions in order to allow the drug to perform its action [33]. Although the MDM2 increase in U-87 MG cells after treatment with nutlin-3a is reported in the literature [27,73], the experimental conditions of those studies considerably differ from those considered in our work as regards

used drug concentration and analyzed time points. Induction, in fact, was observed at earlier or later time points (8–96 h) by using a drug concentration five- to ten-times higher [27,73].

To further confirm that Nut-Mag-SLNs induce cell death through apoptosis regulated by activation of p53 and its transcriptional targets, immunofluorescence was exploited to investigate the precise subcellular localization of p53, p21 and MDM2. Previous works demonstrated that one of the consequences of nutlin-3a-mediated p53 pathway is the nuclear localization of such proteins [74–76]. The translocation of p53 to the nucleus is, in fact, an essential prerequisite to induce apoptosis through transcription-dependent mechanism [74]. p21 is a protein the anti-proliferative functions of which rely on its nuclear localization [77] and, finally, even MDM2 must localize in the nucleus in order to inhibit the p53 transcriptional activity [78]. Our study demonstrates that with respect to the plain drug, Nut-Mag-SLNs induce higher nuclear localization of all investigated proteins owing to the greater ability to activate and stabilize p53 and its downstream targets.

Another aim of the work was investigating Nut-Mag-SLNs ability to cross an *in vitro* BBB model [76]. Obtained results demonstrate that indeed Mag-Nut-SLNs can overcome the developed BBB model by preserving endothelial cells by toxic drug action, and to selectively deliver the drug to GBM cells by causing 50% reduction in cell metabolic activity. This double advantage makes Nut-Mag-SLNs particularly interesting in the field of the drug delivery, where selectively killing tumor cells without affecting healthy cells is one of the primary goals to reduce the side effects of chemotherapy [19].

To investigate the possibility to use the magnetic properties of Nut-Mag-SLNs to foster their accumulation at a target site, we exploited a newly fabricated BBB *in vitro* dynamic model. Magnetic targeting has been widely used during the years as a strategy to externally manipulate and guide drug carries. A recent example is the work by Skouras *et al.* [79], where doxorubicin-loaded magnetoliposomes were used to actively cross an *in vitro* BBB model and to target B16 melanoma cells. Another relevant work was published by Martina *et al.* [80], where magnetic-fluid-loaded liposomes were guided against PC3 adenocarcinoma prostatic cell line. Finally, it is worth to mention the study by Marie *et al.* [81], where magnetic-fluid-loaded-liposomes were targeted toward U87-MG cells implanted in the striatum of mice, thanks to the exposure to an external magnetic field.

A novel two-channel BBB device was designed to further demonstrate the applicability of magnetic targeting, and it represents the first *in vitro* model that permits in a single setup both the study of the ability of candidate therapeutic compounds to cross brain endothelial cells and the analysis of their efficiency on cancer cells. The proposed dynamic BBB system was also fully characterized through physical modeling, so as to enforce the desired wall shear stress and to predict the distribution of magnetic nanostructures on the porous membrane, as induced by an external magnet. Indeed, we experimentally observed Nut-Mag-SLNs accumulation in correspondence of the magnet borders in full agreement with the model. Moreover, accumulated particles were internalized by endothelial cells, crossed the BBB layer (without affecting its integrity), reached cancer cells (seeded in the lower channel), and elicited a cytotoxic effect. Our achievement is therefore twofold: on the one hand, we demonstrated the fascinating possibility to magnetically guide our nanostructures

in a specific area where they can excert their functions in a highly targeted manner; on the other hand, our BBB microfluidic device provides a handy multifunctional platform to foster the accumulation of investigated compounds, their ability to cross the BBB, and their therapeutic effectiveness. However, we have to point out that this model, despite its innovative features, is not intended to be a complete substitute of animal testing, yet rather a complementary tool able to predict fundamental characteristics of candidate therapeutic compounds, like BBB crossing abilities and anti-cancer effects. With the data obtained through the use of our system, a more predictive and reliable screening of drug candidates is possible, thus saving economical resources, time and animals, but unfortunately, this *in vitro* system is still not able to give information about pivotal parameters like drug biodistribution and clearance, lacking the complexity of a whole living organism.

Conclusion

We developed a magnetic drug-delivery system with the aim to increase BBB permeability to anti-tumor compounds, like nutlin-3a, through use of magnetic nanoparticles in tandem with an external magnetic field. Nutlin-3a and SPIONs were encapsulated in SLNs, and *in vitro* experiments confirmed the possibility to magnetically target the nanovectors toward a specific site to cross the BBB and to deliver the drug to GBM cells, thus triggering apoptosis.

Altogether, our results demonstrated that Nut-Mag-SLNs have effective potential for addressing multiple challenges currently open in the field of brain cancer treatment, including the difficulties in delivering drugs across BBB [82], owing to their ability to be magnetically guided toward specific areas and to act as a powerful inhibitor of cancer cell proliferation while harming their viability.

Future perspective

Envisioning clinical studies, mandatory steps in the close future are *in vivo* investigations. Developed nanoparticles will be tested on appropriate animal models (mice implanted with human glioblastoma xenograft), and on these experimental platforms the ‘smartness’ and the multifunctionality of our nanovectors will be tested. The remote guidance based on external magnetic fields would allow the safe accumulation of the nanocarriers at targeted regions within brain tissue, overcoming the limits of invasive release strategies which can compromise the protective role of the BBB. Moreover, features that render our vectors actual ‘theranostic’ devices will be exploited, by using the contrast properties of the SPIONs [83] in order to noninvasively track their localization with magnetic resonance imaging. Finally, the possibility to promote a localized increment of temperature [84] upon applications of alternating magnetic fields will be tested, thus allowing a synergic treatment of the tumor, mediated by both chemotherapy and hyperthermia.

Supplementary Material

Refer to Web version on PubMed Central for supplementary material.

Europe PMC Funders Author Manuscripts

Data availability statement

The datasets generated and/or analyzed during the current study are available from the corresponding author on reasonable request.

References

Papers of special note have been highlighted as: • of interest; •• of considerable interest

1. Piñeros M, Sierra MS, Izarzugaza MI, Forman D. Descriptive epidemiology of brain and central nervous system cancers in Central and South America. Cancer Epidemiol. 2016; 44:S141–S149. [PubMed: 27678316]
2. Araque A, Navarrete M. Glial cells in neuronal network function. Philos Trans Royal Soc B. 2010; 365(1551):2375–2381.
3. Karim R, Palazzo C, Evrard B, Piel G. Nanocarriers for the treatment of glioblastoma multiforme: current state-of-the-art. J Control Rel. 2016; 227:23–37. [•• **A fundamental and complete overview of the main studies concerning the use of nanocarriers in glioblastoma treatment**.]
4. Laks DR, Visnyei K, Kornblum HI. Brain tumor stem cells as therapeutic targets in models of glioma. Yonsei Med J. 2010; 51(5):633–640. [PubMed: 20635435]
5. Yang L, Lin C, Wang L, Guo H, Wang X. Hypoxia and hypoxia-inducible factors in glioblastoma multiforme progression and therapeutic implications. Exp Cell Res. 2012; 318(19):2417–2426. [PubMed: 22906859]
6. Hardee ME, Zagzag D. Mechanisms of glioma-associated neovascularization. Am J Pathol. 2012; 181(4):1126–1141. [PubMed: 22858156]
7. Lima FRS, Kahn SA, Soletti RC, et al. Glioblastoma: therapeutic challenges, what lies ahead. Biochim Biophys Acta. 2012; 1826(2):338–349. [PubMed: 22677165]
8. Cheng L, Bao S, Rich JN. Potential therapeutic implications of cancer stem cells in glioblastoma. Biochem Pharmacol. 2010; 80(5):654–665. [PubMed: 20457135]
9. Fang C, Wang K, Stephen ZR. Temozolomide nanoparticles for targeted glioblastoma therapy. ACS Appl Mater Interfaces. 2015; 7(12):6674–6682. [PubMed: 25751368]
10. Zhou Y, Peng Z, Seven ES, Leblanc RM. Crossing the blood–brain barrier with nanoparticles. J Control Rel. 2018; 270:290–303. [• **An extensive analysis of traditional and innovative nanoparticles systems for drug delivery across the blood–brain barrier**.]
11. Abbott NJ, Rönnbäck L, Hansson E. Astrocyte-endothelial interactions at the blood–brain barrier. Nat Rev Neurosci. 2006; 7(1):41–53. [PubMed: 16371949]
12. Banerjee J, Shi Y, Azevedo HS. *In vitro* blood–brain barrier models for drug research: state-of-the-art and new perspectives on reconstituting these models on artificial basement membrane platforms. Drug Discov Today. 2016; 21(9):1367–1386. [PubMed: 27283274] [•• **A complete review about blood–brain barrier *in vitro* models currently present in the literature**.]
13. Ramirez YP, Weatherbee JL, Wheelhouse RT, Ross AH. Glioblastoma multiforme therapy and mechanisms of resistance. Pharm. 2013; 6(12):1475–1506.
14. Ganipineni LP, Danhier F, Préat V. Drug delivery challenges and future of chemotherapeutic nanomedicine for glioblastoma treatment. J Control Rel. 2018; 281:42–57.
15. Oberoi RK, Parrish KE, Sio TT, Mittapalli RK, Elmquist WF, Sarkaria JN. Strategies to improve delivery of anticancer drugs across the blood–brain barrier to treat glioblastoma. Neuro-oncol. 2016; 18(1):27–36. [PubMed: 26359209]
16. Pourgholi F, Hajivalili M, Farhad JN, Kafil HS, Yousefi M. Nanoparticles: novel vehicles in treatment of glioblastoma. Biomed Pharmacother. 2016; 77:98–107. [PubMed: 26796272]
17. Cerna T, Stiborova M, Adam V, Kizek R, Eckschlager T. Nanocarrier drugs in the treatment of brain tumors. JCMT. 2016; 2(10):407.
18. Tsou YH, Zhang XQ, Zhu H, Syed S, Xu X. Drug delivery to the brain across the blood-brain barrier using nanomaterials. Small. 2017; 13(43):1–17.

19. Wicki A, Witzigmann D, Balasubramanian V, Huwyler J. Nanomedicine in cancer therapy: challenges, opportunities, and clinical applications. J Control Rel. 2015; 200:138–157.
20. Jain K. Use of nanoparticles for drug delivery in glioblastoma multiforme. Expert Rev Neurother. 2007; 7(4):363–372. [PubMed: 17425491]
21. Ling Y, Wei K, Zou F, Zhong S. Use of nanoparticles for drug delivery in glioblastoma multiforme. Int J Pharm. 2012; 430(1–2):266–275. [PubMed: 22486964]
22. Nordling-David MM, Yaffe R, Guez D, et al. Liposomal temozolomide drug delivery using convection enhanced delivery. J Control Rel. 2017; 261:138–146.
23. Xin H, Sha X, Jiang X, Zhang W, Chen L, Fang X. Anti-glioblastoma efficacy and safety of paclitaxel-loading angiopep-conjugated dual targeting PEG-PCL nanoparticles. Biomaterials. 2012; 33(32):8167–8176. [PubMed: 22889488]
24. Ambruosi A, Gelperina S, Khalansky A, Tanski S, Theisen A, Kreuter J. Influence of surfactants, polymer and doxorubicin loading on the anti-tumour effect of poly(butyl cyanoacrylate) nanoparticles in a rat glioma model. J Microencapsul. 2006; 23(5):582–592. [PubMed: 16980278]
25. Although B. Nanobiotechnology-based strategies for crossing the blood–brain barrier. Nanomedicine. 2012; 7:1225–1233. [PubMed: 22931448]
26. Grillone A, Ciofani G. Magnetic nanotransducers in biomedicine. Chem Eur J. 2017; 23(64):16109–16114. [PubMed: 28922494]
27. Villalonga-Planells R, Coll-Mulet L, Martìnez-Soler F, et al. Activation of p53 by nutlin-3a induces apoptosis and cellular senescence in human glioblastoma multiforme. PLoS ONE. 2011; 6(4):e18588. [PubMed: 21483692]
28. Wang B, Fang L, Zhao H, Xiang T, Wan D. MDM2 inhibitor Nutlin-3a suppresses proliferation and promotes apoptosis in osteosarcoma cells. Acta Biochim Biophys Sin. 2012; 44(8):685–691. [PubMed: 22843172]
29. Janouskova H, Ray AM, Noulet F, et al. Activation of p53 pathway by nutlin-3a inhibits the expression of the therapeutic target α5 integrin in colon cancer cells. Cancer Lett. 2013; 336(2):307–318. [PubMed: 23523610] [• **An interesting work about the role of nutlin in the p53 pathway in colon cancer**.]
30. Manfé V, Biskup E, Johanse P, et al. MDM2 inhibitor nutlin-3a induces apoptosis and senescence in cutaneous T-cell lymphoma: role of p53. J Investig Dermatol. 2012; 132(5):1487–1496. [PubMed: 22377766]
31. Valente LJ, Aubrey BJ, Herold MJ, et al. Therapeutic response to non-genotoxic activation of p53 by nutlin3a is driven by PUMA-mediated apoptosis in lymphoma cells. Cell Rep. 2016; 14(8):1858–1866. [PubMed: 26904937]
32. Saha MN, Qiu L, Chang H. Targeting p53 by small molecules in hematological malignancies. J Hem Oncol. 2013; 6(1):1.
33. Zhao Y, Aguilar A, Bernard D, Wang SJ. Small-molecule inhibitors of the MDM2–p53 protein–protein interaction (MDM2 inhibitors) in clinical trials for cancer treatment. Med Chem. 2015; 58(3):1038–1052.
34. Crespo I, Vital AL, Gonzalez-Tablas M, et al. Molecular and genomic alterations in glioblastoma multiforme. Am J Pathol. 2015; 185(7):1820–1833. [PubMed: 25976245]
35. Gu L, Zhu N, Findley HW, Zhou M. MDM2 antagonist nutlin-3 is a potent inducer of apoptosis in pediatric acute lymphoblastic leukemia cells with wild-type p53 and overexpression of MDM2. Leukemia. 2008; 22(4):730–739. [PubMed: 18273046]
36. Vassilev LT, Vu BT, Craves B, et al. *In vivo* activation of the p53 pathway by small-molecule antagonists of MDM2. Science. 2004; 303(5659):844–848. [PubMed: 14704432]
37. Das M, Sahoo SK. Folate decorated dual drug loaded nanoparticle: role of curcumin in enhancing therapeutic potential of nutlin-3a by reversing multidrug resistance. PLoS ONE. 2012; 7(3):e32920. [PubMed: 22470431]
38. Das M, Dilnawaz F, Sahoo SK. Targeted nutlin-3a loaded nanoparticles inhibiting p53-MDM2 interaction: novel strategy for breast cancer therapy. Nanomedicine. 2011; 6(3):489–507. [PubMed: 21542687]

39. Ribecco-Lutkiewicz M, Sodja C, Haukenfrers J, et al. A novel human induced pluripotent stem cell blood–brain barrier model: applicability to study antibody-triggered receptor-mediated transcytosis. Sci Rep. 2018; 8(1):1–17. [PubMed: 29311619]
40. Emeule MD, Hedid DS. Expression of multidrug-resistance P-glycoprotein (MDR1) in human brain tumors. Int J Cancer. 2001; 93(1):62–66. [PubMed: 11391622]
41. Battaglia L, Gallarate M, Peira E, et al. Solid lipid nanoparticles for potential doxorubicin delivery in glioblastoma treatment: preliminary *in vitro* studies. J Pharm Sciences. 2014; 103(7):2157–2165.
42. Kaur IP, Bhandari R, Bhandari S, Kakkar V. Potential of solid lipid nanoparticles in brain targeting. J Control Rel. 2008; 127(2):97–109.
43. Tapeinos C, Battaglini M, Ciofani G. Advances in the design of solid lipid nanoparticles and nanostructured lipid carriers for targeting brain diseases. J Control Rel. 2017; 264:306–332.
44. Bang S, Lee SR, Ko J, et al. A low permeability microfluidic blood–brain barrier platform with direct contact between perfusable vascular network and astrocytes. Sci Rep. 2017; 7(1):8083. [PubMed: 28808270]
45. Booth, RH; Kim, HA. A parallel array microfluidic blood–brain barrier model for high-throughput quantitation of shear stress effects. 16th International Conference on Miniaturized Systems for Chemistry and Life Sciences; 2012. 491–493.
46. Wang YI, Abaci HE, Shuler ML. Microfluidic blood–brain barrier model provides *in vivo*-like barrier properties for drug permeability screening. Biotechnol Bioeng. 2017; 114(1):184–194. [PubMed: 27399645]
47. Cucullo L, Marchi N, Hossain M, Janigro D. A dynamic *in vitro* BBB model for the study of immune cell trafficking into the central nervous system. J Cereb Blood Flow Metab. 2010; 31(2):767–777. [PubMed: 20842162]
48. Takeshita Y, Obermeier B, Cotleur A, Sano Y, Kanda T, Ransohoff RM. An *in vitro* blood–brain barrier model combining shear stress and endothelial cell/astrocyte co-culture. J Neurosci Methods. 2014; 232:165–172. [PubMed: 24858797]
49. Adriani G, Ma D, Pavesi A, et al. A 3D neurovascular microfluidic model consisting of neurons, astrocytes and cerebral endothelial cells as a blood–brain barrier. Lab Chip. 2017; 12(3):169–182.
50. Adriani G, Ma D, Pavesi A, Goh ELK, Kamm RD. Modeling the blood–brain barrier in a 3D triple co-culture microfluidic system. Conf Proc IEEE Eng Med Biol Soc EMBS. 2015:338–341.
51. Prabhakarpandian B, Shen MC, Nichols JB, et al. SyM-BBB: a microfluidic blood-brain barrier model. Lab Chip. 2013; 13(6):1093–1101. [PubMed: 23344641] [•• **Work about the design of an *in vitro* microfluidic blood–brain barrier model, still a reference point in the field of *in vitro* modeling of biological systems**.]
52. Walter FR, Valkai S, Kincses A, et al. A versatile lab-on-a-chip tool for modeling biological barriers. Sens Actuators B: Chem. 2016; 222:1209–1219.
53. Partyka PP, Godsey GA, Galie JR. Mechanical stress regulates transport in a compliant 3D model of the blood-brain barrier. Biomaterials. 2017; 115:30–39. [PubMed: 27886553]
54. Achyuta AKH, Conway AJ, Crouse RB, et al. A modular approach to create a neurovascular unit-on-a-chip. Lab Chip. 2013; 13(4):542–553. [PubMed: 23108480]
55. Wong AD, Ye M, Levy AF, Rothstein JD, Bergles DE, Searson PC. The blood–brain barrier: an engineering perspective. Front Neuroeng. 2013; 6:1–22. [PubMed: 23443302]
56. Berselli LC, Miloro P, Menciassi A, Sinibaldi E. Exact solution to the inverse Womersley problem for pulsatile flows in cylindrical vessels, with application to magnetic particle targeting. Appl Math Comput. 2013; 219(10):5717–5729.
57. Knobel M, Nunes WC, Socolovsky LM, De Biasi E, Vargas JM. Superparamagnetism and other magnetic features in granular materials: a review on ideal and real systems. J Nanosci Nanotechnol. 2008; 8(4):2836–2857. [PubMed: 18681019]
58. Bean CP, Livingston JD. Superparamagnetism. J Appl Phys. 1959; 30(4):S120–S129.
59. Lowe SW, Lin AW. Apoptosis in cancer. Carcinogenesis. 2000; 21(3):485–495. [PubMed: 10688869]

Europe PMC Funders Author Manuscripts

60. Omidi Y, Campbell L, Barar J, Connell D, Akhtar S, Gumbleton M. Evaluation of the immortalised mouse brain capillary endothelial cell line, b.End3, as an *in vitro* blood–brain barrier model for drug uptake and transport studies. Brain Res. 2003; 990(1–2):95–112. [PubMed: 14568334]
61. Gaillard PJ, de Boer AG. Relationship between permeability status of the blood–brain barrier and *in vitro* permeability coefficient of a drug. Eur J Pharm Sci. 2000; 12(2):95–102. [PubMed: 11102736]
62. Muradashvili N, Tyagi R, Lominadze D. A dual-tracer method for differentiating transendothelial transport from paracellular leakage *in vivo* and *in vitro* . Front Physiol. 2012; 3:166. [PubMed: 22754530]
63. Brown RC, Morris AP, O'Neil RG. Tight junction protein expression and barrier properties of immortalized mouse brain microvessel endothelial cells. Brain Res. 2007; 1130:17–30. [PubMed: 17169347]
64. Belletti D, Tosi G, Riv G, et al. Nutlin-3 loaded nanocarriers: preparation, characterization and *in vitro* antineoplastic effect against primary effusion lymphoma. Int J Pharm. 2015; 490(1–2):85–93. [PubMed: 25987470]
65. Voltan R, Secchiero P, Ruozi B, et al. Nanoparticles engineered with rituximab and loaded with nutlin-3 show promising therapeutic activity in B-leukemic xenografts. Clin Cancer Res. 2013; 19(14):3871–3880. [PubMed: 23719263]
66. Jokerst JV, Lobovkina T, Zare RN, Gambhir SS. Nanoparticle PEGylation for imaging and therapy. Nanomedicine. 2011; 6(4):715–728. [PubMed: 21718180]
67. Saraiva C, Praña C, Ferreira R, Santos T, Ferreira L, Bernardino L. Nanoparticle-mediated brain drug delivery: overcoming blood-brain barrier to treat neurodegenerative diseases. J Control Rel. 2016; 235:34–47.
68. Patel MM, Patel BM. Crossing the blood–brain barrier: recent advances in drug delivery to the brain. CNS Drugs. 2017; 31(2):109–133. [PubMed: 28101766]
69. Kang KW, Chun MK, Kim O, et al. Doxorubicin-loaded solid lipid nanoparticles to overcome multidrug resistance in cancer therapy. Nanomedicine. 2010; 6(2):210–213. [PubMed: 20060074]
70. Radaic A, De Jesus MB. Solid lipid nanoparticles release DNA upon endosomal acidification in human embryonic kidney cells. Nanotechnology. 2018; 29(31)
71. Miyachi M, Kakazu N, Yagyu S, et al. Restoration of p53 pathway by nutlin-3 induces cell cycle arrest and apoptosis in human rhabdomyosarcoma cells. Clin Cancer Res. 2009; 15(12):4077–4084. [PubMed: 19509161]
72. Halatsch ME, Schmidt U, Unterberg A, Vougioukas VI. Uniform MDM2 overexpression in a panel of glioblastoma multiforme cell lines with divergent EGFR and p53 expression status. Anticancer Res. 2006; 26(6B):4191–4194. [PubMed: 17201132]
73. Wang H, Cai S, Bailey BJ, et al. Combination therapy in a xenograft model of glioblastoma: enhancement of the antitumor activity of temozolomide by an MDM2 antagonist. J Neurosurg. 2017; 126(2):446–459. [PubMed: 27177180]
74. Elison JR, Cobrinik D, Claros N, Abramson DH, Lee TC. Small molecule inhibition of HDM2 leads to p53-mediated cell death in retinoblastoma cells. Arch Ophthalmol. 2006; 124(9):1269–1275. [PubMed: 16966622]
75. Kojima K, Konopleva M, Samudio IJ, Ruvolo V, Andreeff M. Mitogen-activated protein kinase kinase inhibition enhances nuclear proapoptotic function of p53 in acute myelogenous leukemia cells. Cancer Res. 2007; 67(7):3210–3219. [PubMed: 17409429]
76. Shen H, Maki CG. Persistent p21 expression after nutlin-3a removal is associated with senescence-like arrest in 4N cells. J Biol Chem. 2010; 285(30):23105–23114. [PubMed: 20489208]
77. Moll UM, Petrenko O. The MDM2-p53 interaction. Mol Cancer Res. 2003; 1(14):1001–1008. [PubMed: 14707283] [• **Important work that highlights the murine double minute/p53 interaction**.]
78. Child ES, Mann DJ. The intricacies of p21 phosphorylation: protein/protein interactions, subcellular localization and stability. Cell Cycle. 2006; 5(12):1313–1319. [PubMed: 16775416]
79. Skouras A, Papadia K, Mourtas S, Klepetsanis P, Antimisiaris SG. Multifunctional doxorubicin-loaded magnetoliposomes with active and magnetic targeting properties. Eur J Pharm Sci. 2018; 123:162–172. [PubMed: 30041027]

80. Martina MS, Wilhelm C, Lesieur S. The effect of magnetic targeting on the uptake of magnetic-fluid-loaded liposomes by human prostatic adenocarcinoma cells. Biomaterials. 2008; 29(30):4137–4145. [PubMed: 18667235]

81. Marie H, Lemaire L, Franconi F, et al. Superparamagnetic liposomes for MRI monitoring and external magnetic field-induced selective targeting of malignant brain tumors. Adv Funct Mater. 2015; 25(8):1258–1269.

82. Pardridge WM. The blood–brain barrier: bottleneck in brain drug development. NeuroRx. 2005; 2(1):3–14. [PubMed: 15717053] [•• **One of the most complete analyses on the obstacle that blood–brain barrier poses to brain drug delivery**.]

83. Mosayebi J, Kiyasatfar M, Laurent S. Synthesis, functionalization, and design of magnetic nanoparticles for theranostic applications. Advanc Health Mat. 2017; 6(23)

84. Muñoz de Escalona M, Sáez-Fernández E, Prados JC, Melguizo C, Arias JL. Magnetic solid lipid nanoparticles in hyperthermia against colon cancer. Int J Pharm. 2017; 504(1–2):11–19.

Europe PMC Funders Author Manuscripts

Europe PMC Funders Author Manuscripts

Summary points

- Glioblastoma multiforme (GBM) is one of the most aggressive forms of cancer currently without any available treatment.
- One of the most challenging problems in the treatment of GBM is the presence of the blood–brain barrier (BBB), a continuous barrier that envelopes brain blood vessels and blocks the passage of many therapeutic compounds.
- Nanomaterials can be used as a carrier system to overcome the obstacles posed by the BBB. In particular, solid lipid nanoparticles (SLNs), thanks to their characteristics in term of stability, biocompatibility and drug release profile, represent an optimal candidate for brain drug delivery.
- Nutlin-loaded magnetic solid lipid nanoparticles (Nut-Mag-SLNs) were fabricated and characterized in terms of size, morphology, stability, drug-loaded content and magnetic properties.
- Two different BBB *in vitro* models have been developed, a static model composed by bEnd.3 brain endothelial cells seeded on a transwell insert and an innovative microfluidic model composed of two chambers resembling the luminal and the abluminal compartments in the tumor microenvironment.
- Nut-Mag-SLNs demonstrated higher anti-cancer ability with respect to the plain drug. Analysis performed through immunofluorescence and western blotting revealed that p53, MDM2 and p21 are involved upon the Nut-Mag-SLNs treatment.
- Nut-Mag-SLNs were able to cross the BBB *in vitro* models; moreover, by exploiting a remote magnetic field the accumulation of the particles was promoted, allowing achieving local concentrations high enough to promote apoptosis of cancer cells without harming endothelial cells.
- Nut-Mag-SLNs represent a promising multifunctional nanoplatform for brain drug delivery and glioblastoma treatment.

Europe PMC Funders Author Manuscripts

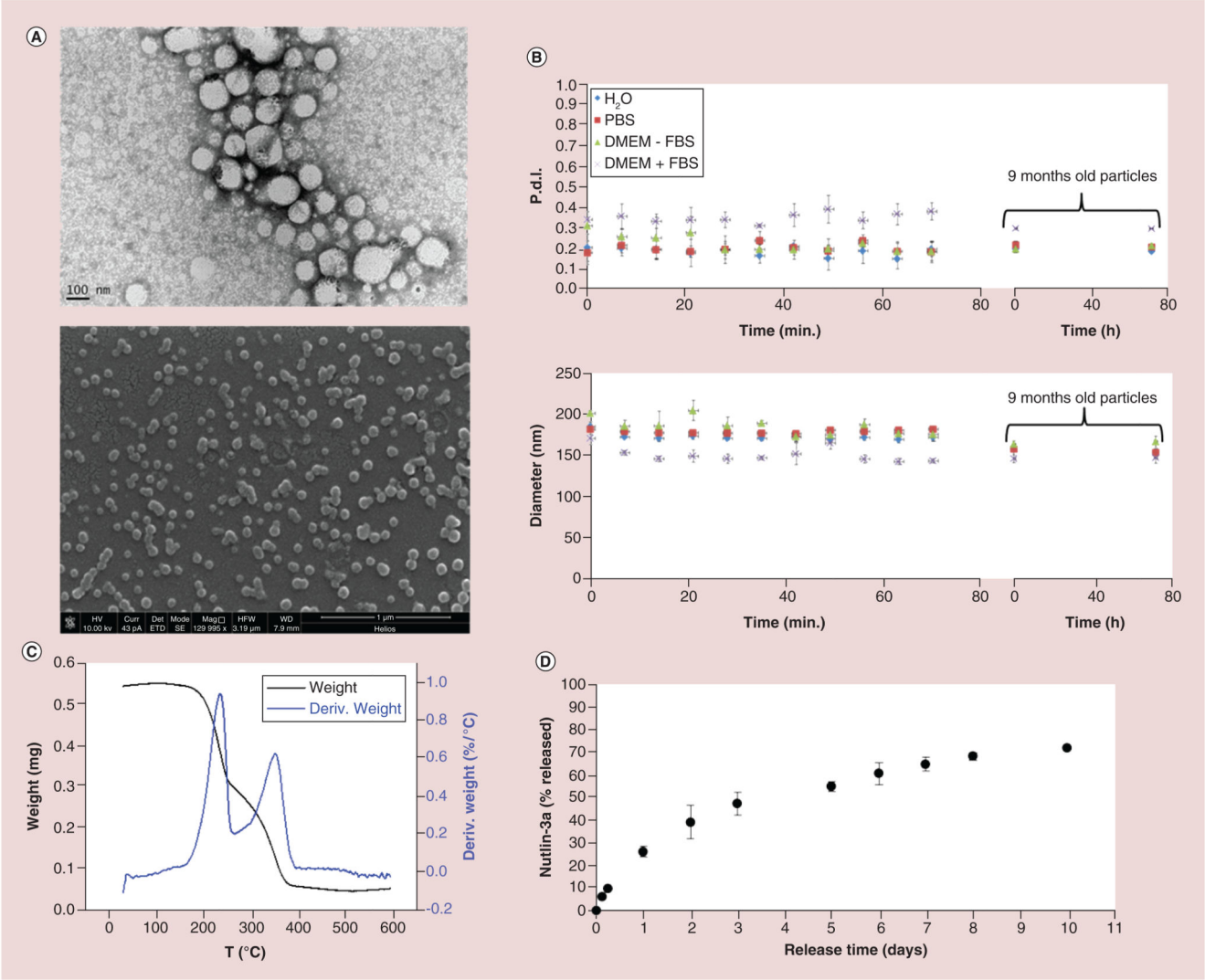

Figure 1. Characterization of nutlin-loaded magnetic solid lipid nanoparticles.

(A) Transmission electron microscopy (top) and scanning electron microscopy (bottom) images of Nut-Mag-SLNs. **(B)** Short- and long-term stability studies of Nut-Mag-SLNs: hydrodynamic diameter (top) and polydispersity index (bottom) in different media. **(C)** Thermogravimetric analysis performed to evaluate of the amount of magnetic nanoparticles loaded in Nut-Mag-SLNs. **(D)** Drug release profile of nutlin-3a from Nut-Mag-SLNs in PBS at pH 7.4.

FBS: Fetal bovine serum; Nut-Mag-SLNs: Nutlin-loaded magnetic solid lipid nanoparticles; PBS: Phosphate-buffered saline.

Europe PMC Funders Author Manuscripts

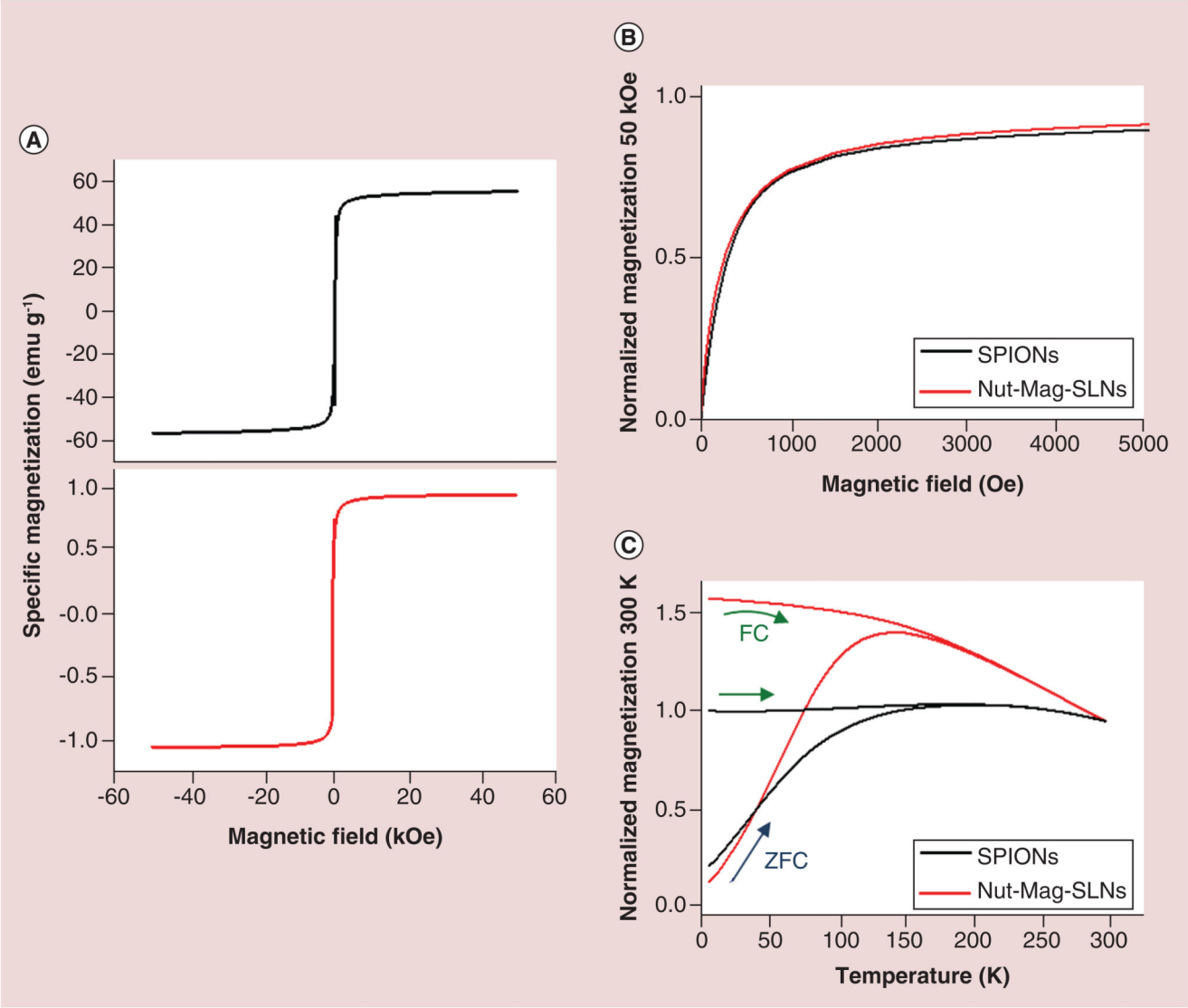

Figure 2. Magnetic characterization of nutlin-loaded magnetic solid lipid nanoparticles.

(A) Hysteresis loops of the bare SPIONs (top) and of the Mag-SLNs (bottom) measured at room temperature. **(B)** Normalized magnetization as function of the field in the low field region of the bare SPIONs and of the Nut-Mag-SNLs. The normalization was done with the respect to the magnetization measured at 50 kOe. **(C)** Temperature dependence of the normalized magnetization of the bare SPIONs and of the Nut-Mag-SNLs using the ZFC and FC procedures. The normalization was performed at the magnetization value at room temperature.

FC: Field-cooling; Mag-SLNs: Magnetic solid lipid nanoparticles; Nut-Mag-SNLs: Nutlin-loaded magnetic solid lipid nanoparticles; SPIONs: Superparamagnetic iron oxide nanoparticles; ZFC: Zero-field-cooling.

Europe PMC Funders Author Manuscripts

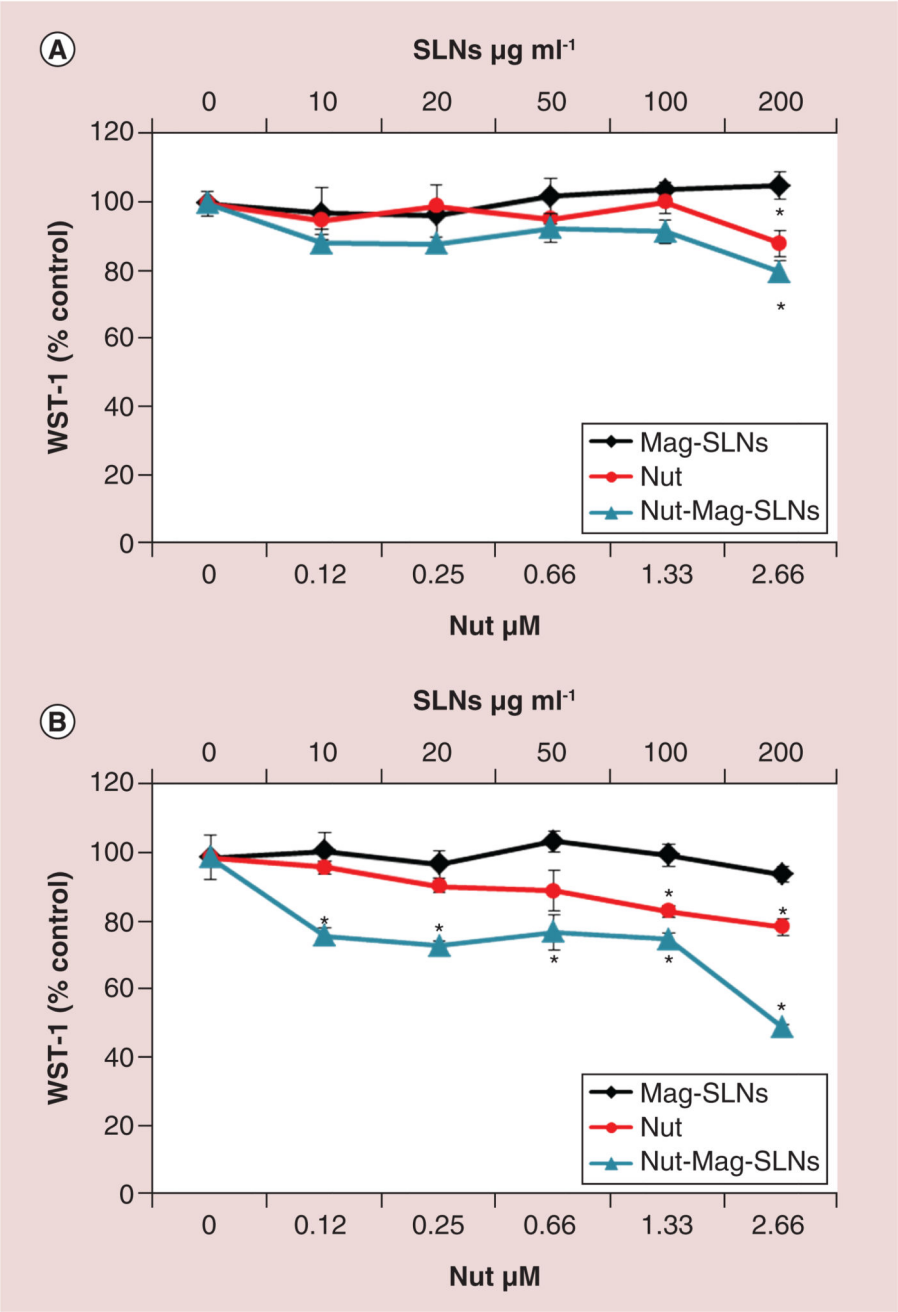

Figure 3. Cytotoxicity study through WST-1 assay.

Metabolic activity of U-87 MG cells after 24 **(A)** and 72 h **(B)** of incubation with increasing concentrations of Mag-SLNs, Nut-Mag-SLNs and free nutlin-3a.

*$p < 0.05$.

Mag-SLNs: Magnetic solid lipid nanoparticles; Nut-Mag-SNLs: Nutlin-loaded magnetic solid lipid nanoparticles.

Europe PMC Funders Author Manuscripts

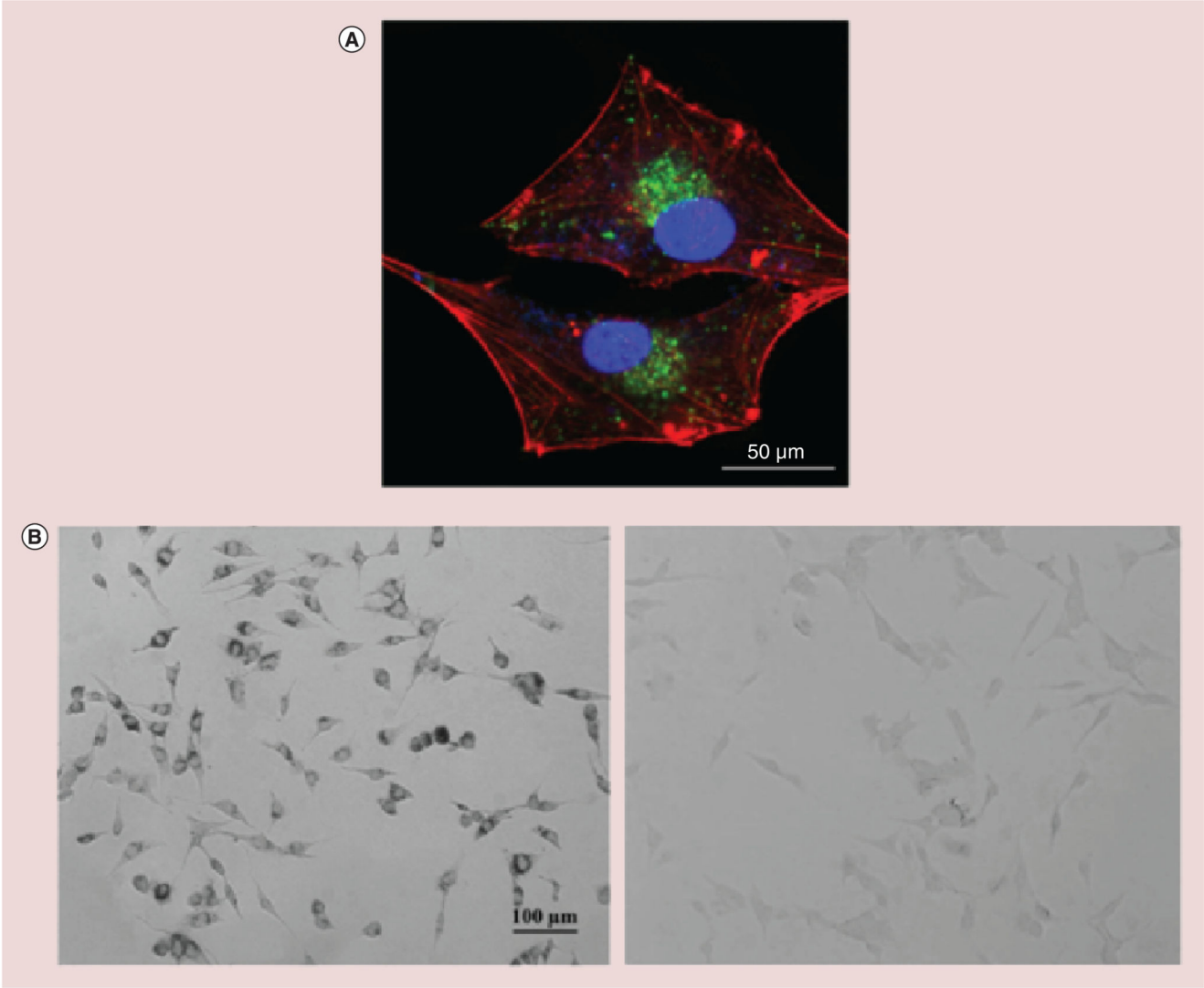

Figure 4. Cellular uptake investigation.

(A) Representative confocal fluorescence image of U-87 MG cells showing FITC-Nut-Mag-SLNs uptake after 24 h of incubation (nanoparticles in green, f-actin in red, nuclei in blue). **(B)** Prussian blue staining of U-87 MG cells after 24 h of incubation with Nut-Mag-SLNs (on the left). The image shows blue precipitates in the perinuclear area due to the presence of SPIONs upon Nut-Mag-SLN internalization. Nontreated cells are reported as control (on the right).

Nut-Mag-SNLs: Nutlin-loaded magnetic solid lipid nanoparticles; SPIONs: Superparamagnetic iron oxide nanoparticles.

Europe PMC Funders Author Manuscripts

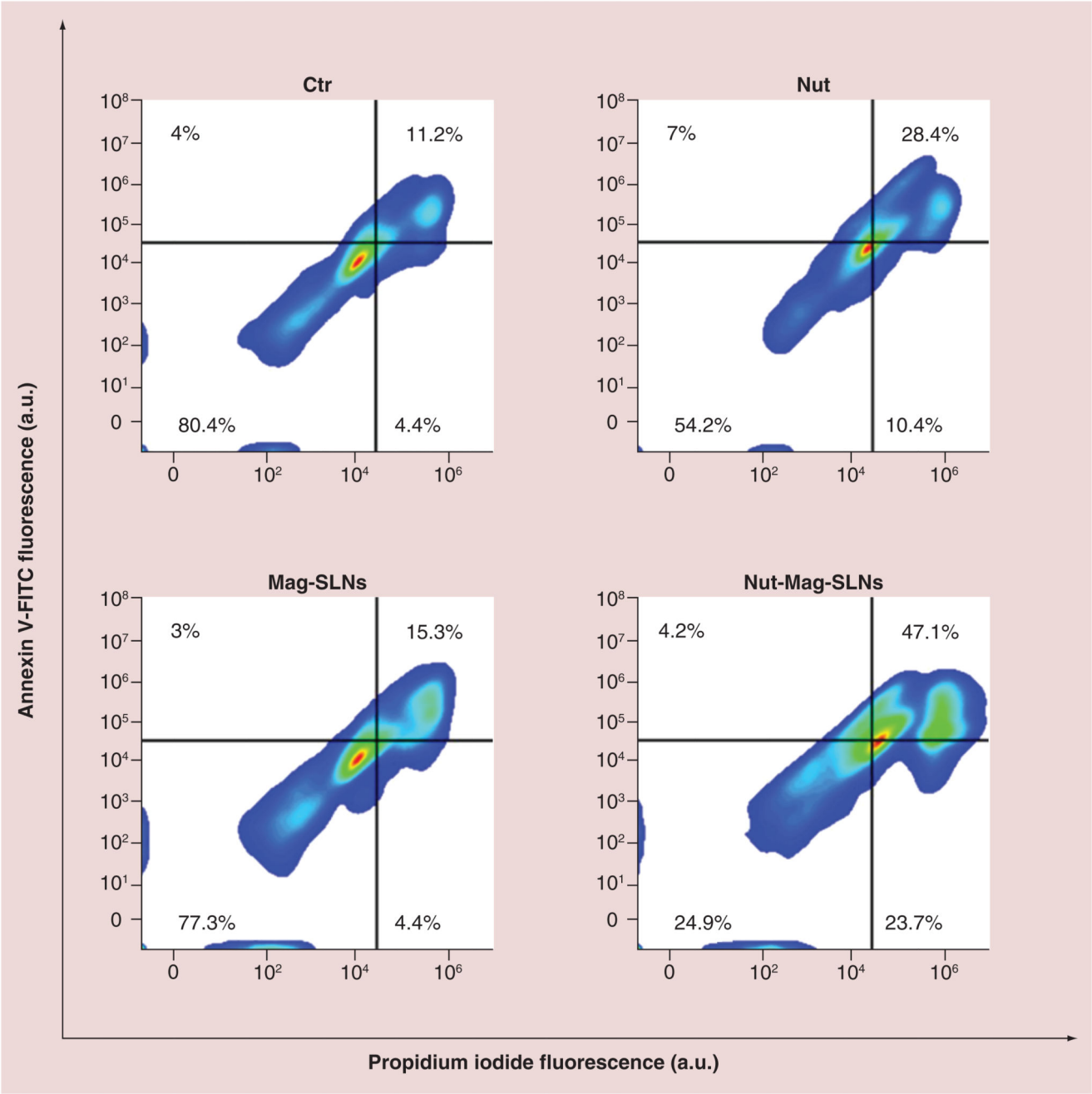

Figure 5. Flow-cytometry evaluation of apoptosis/necrosis.

U-87 MG cells were treated with 100 μg ml^{-1} of Mag-SLNs, 1.33 μM of free nutlin-3a, or 100 μg ml^{-1} of Nut-Mag-SLNs (corresponding to 1.33 μM of drug) for 72 h, and compared with control cultures. Apoptosis and necrosis percentages were measured by using standard annexin V-FITC/propidium iodide staining.

Mag-SLNs: Magnetic solid lipid nanoparticles; Nut-Mag-SNLs: Nutlin-loaded magnetic solid lipid nanoparticles. FITC: Fluorescein isothiocyanate.

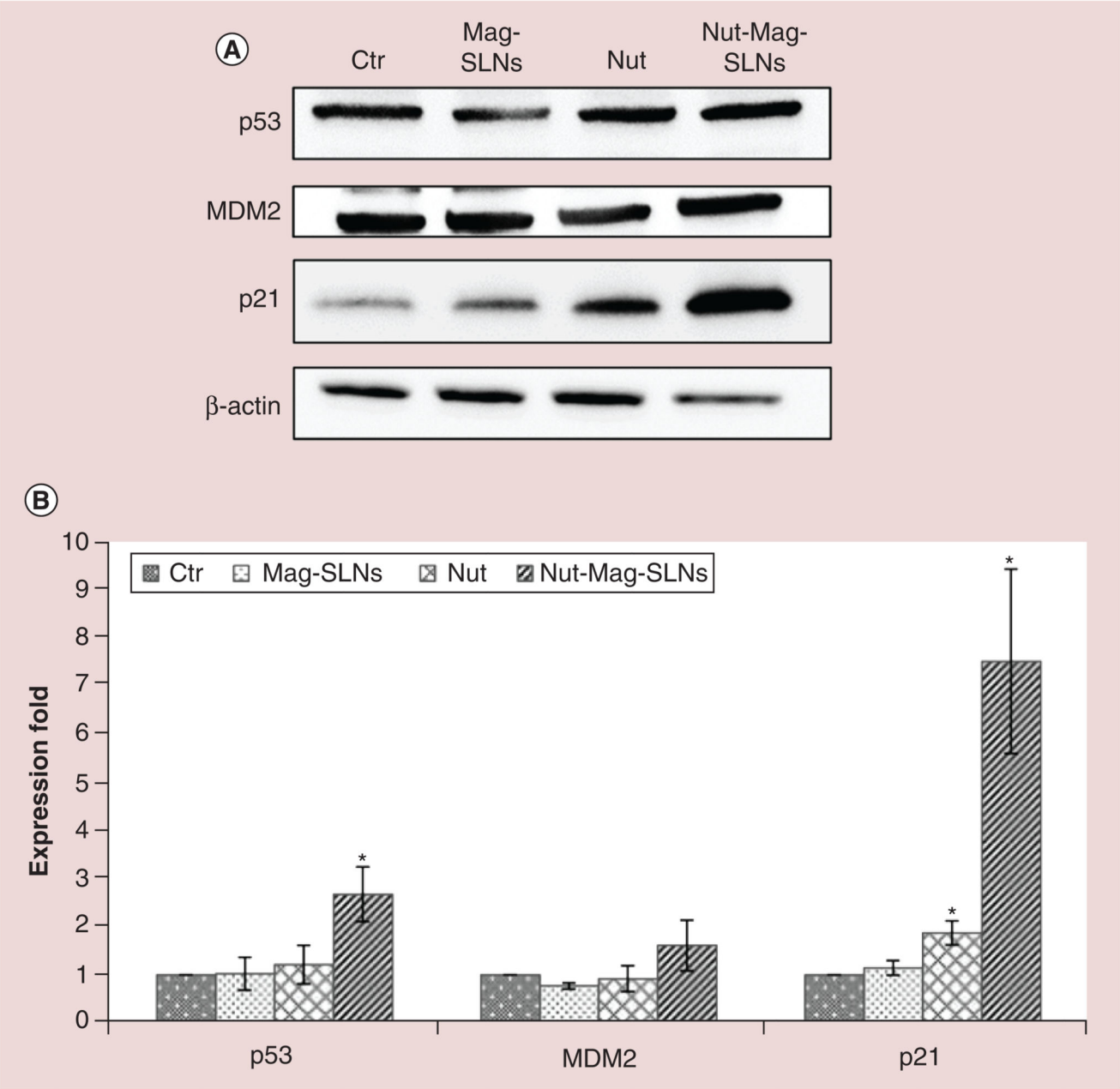

Figure 6. Western blotting analysis of markers involved in apoptosis.

(A) Expression of p53 and its downstream proteins (MDM2 and p21) was analyzed on U-87 MG cells after 72 h of treatment with 100 μg ml^{-1} of Mag-SLNs, 1.33 μM of nutlin-3a, or 100 μg ml^{-1} of Nut-Mag-SLNs (corresponding to 1.33 μM of drug), and compared with control cultures. **(B)** Quantitative evaluation of western blotting results.

*$p < 0.01$.

MDM2: Murine double minute; Mag-SLNs: Magnetic solid lipid nanoparticles; Nut-Mag-SNLs: Nutlin-loaded magnetic solid lipid nanoparticles.

Europe PMC Funders Author Manuscripts

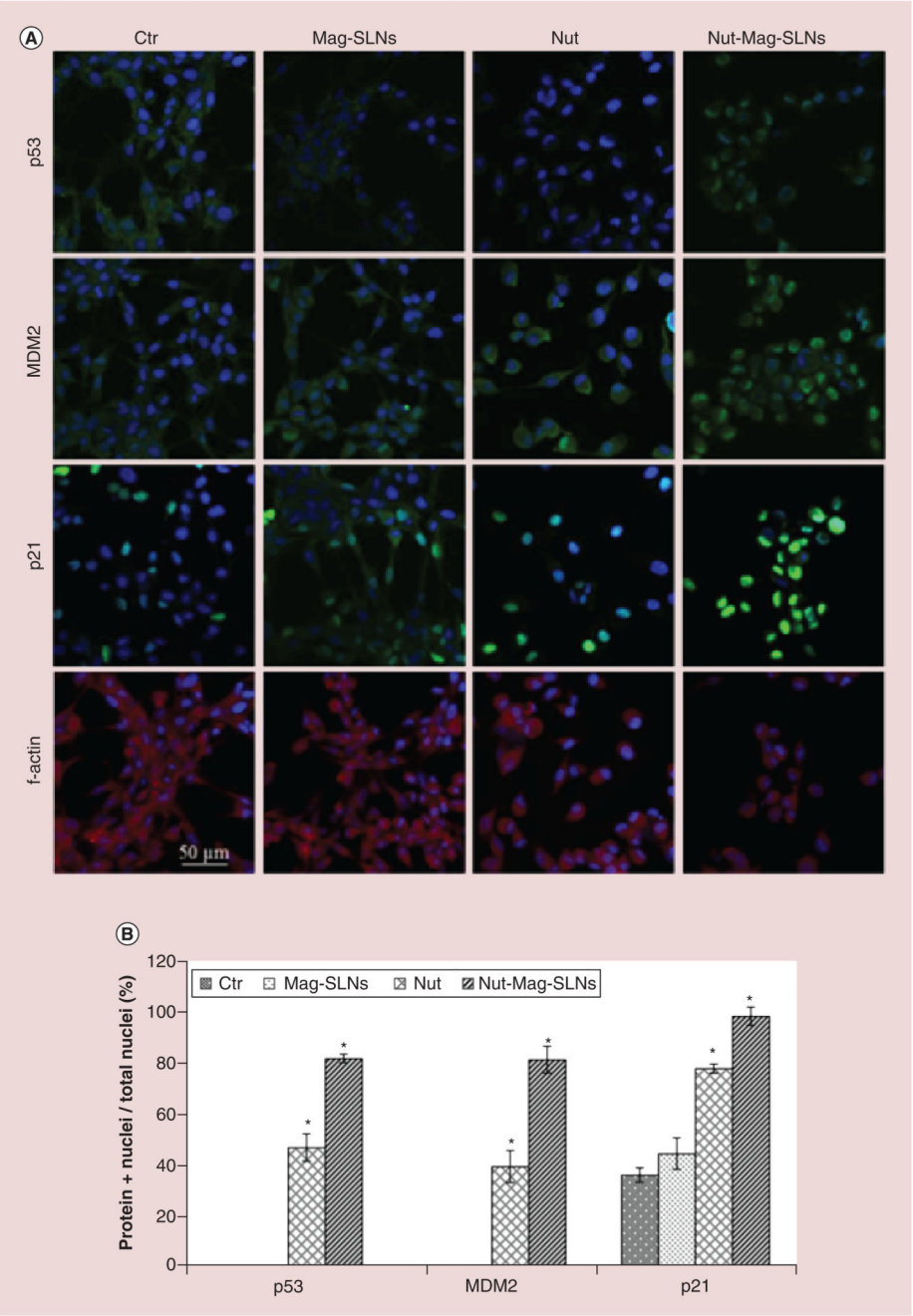

Figure 7. Immunofluorescence analysis of markers involved in apoptosis.

(A) p53, MDM2 and p21 subcellular localization highlighted by immunofluorescence in U-87 MG cells following the treatment with 100 μg ml^{-1} of Mag-SLNs, 1.33 μM of nutlin-3a, or 100 μg ml^{-1} of Nut-Mag-SLNs (corresponding to 1.33 μM of drug), and compared with control cultures (f-actin in red, nuclei in blue, p53/MDM2/p21 in green. **(B)** Quantitative evaluation of cell nuclei positive for p53, MDM2 and p21.

*$p < 0.05$.

MDM2: Murine double minute; Mag-SLNs: Magnetic solid lipid nanoparticle; Nut-Mag-SNLs: Nutlin-loaded magnetic solid lipid nanoparticles.

Europe PMC Funders Author Manuscripts

Europe PMC Funders Author Manuscripts

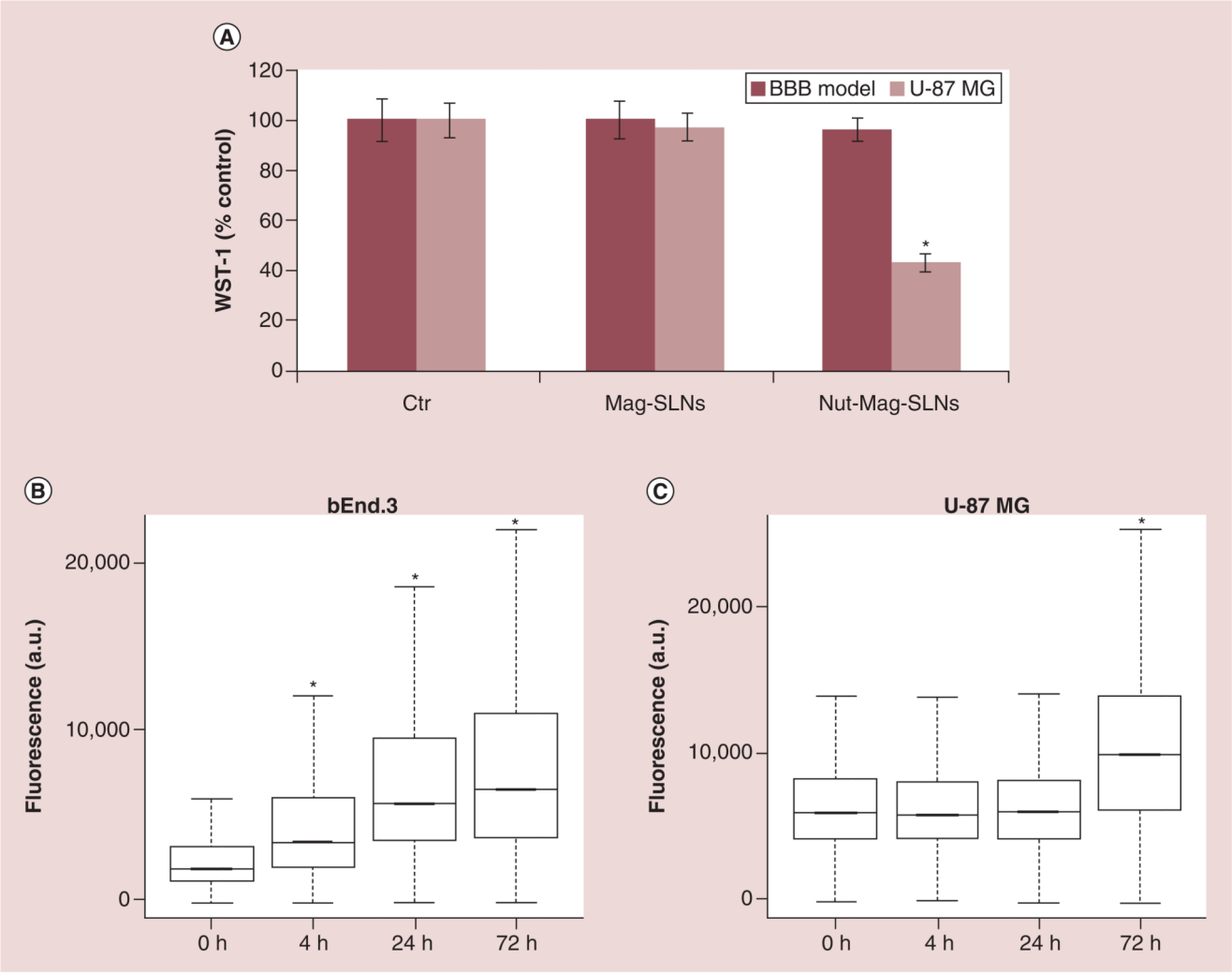

Figure 8. Nutlin-loaded magnetic solid lipid nanoparticles crossing of the *in vitro* blood–brain barrier model.

(A) Metabolic WST-1 assay on BBB model (600 μg ml^{-1}) and on U-87 MG cells (200 μg ml^{-1}) after treatment with Mag-SLNs and Nut-Mag-SLNs. **(B, C)** Flow cytometry evaluation of FITC-Nut-Mag-SLN uptake by bEnd.3 and U-87 MG cells at different time points.

*$p < 0.05$.

BBB: Blood–brain barrier; Mag-SLNs: Magnetic solid lipid nanoparticles; Nut-Mag-SNLs: Nutlin-loaded magnetic solid lipid nanoparticles.

Europe PMC Funders Author Manuscripts

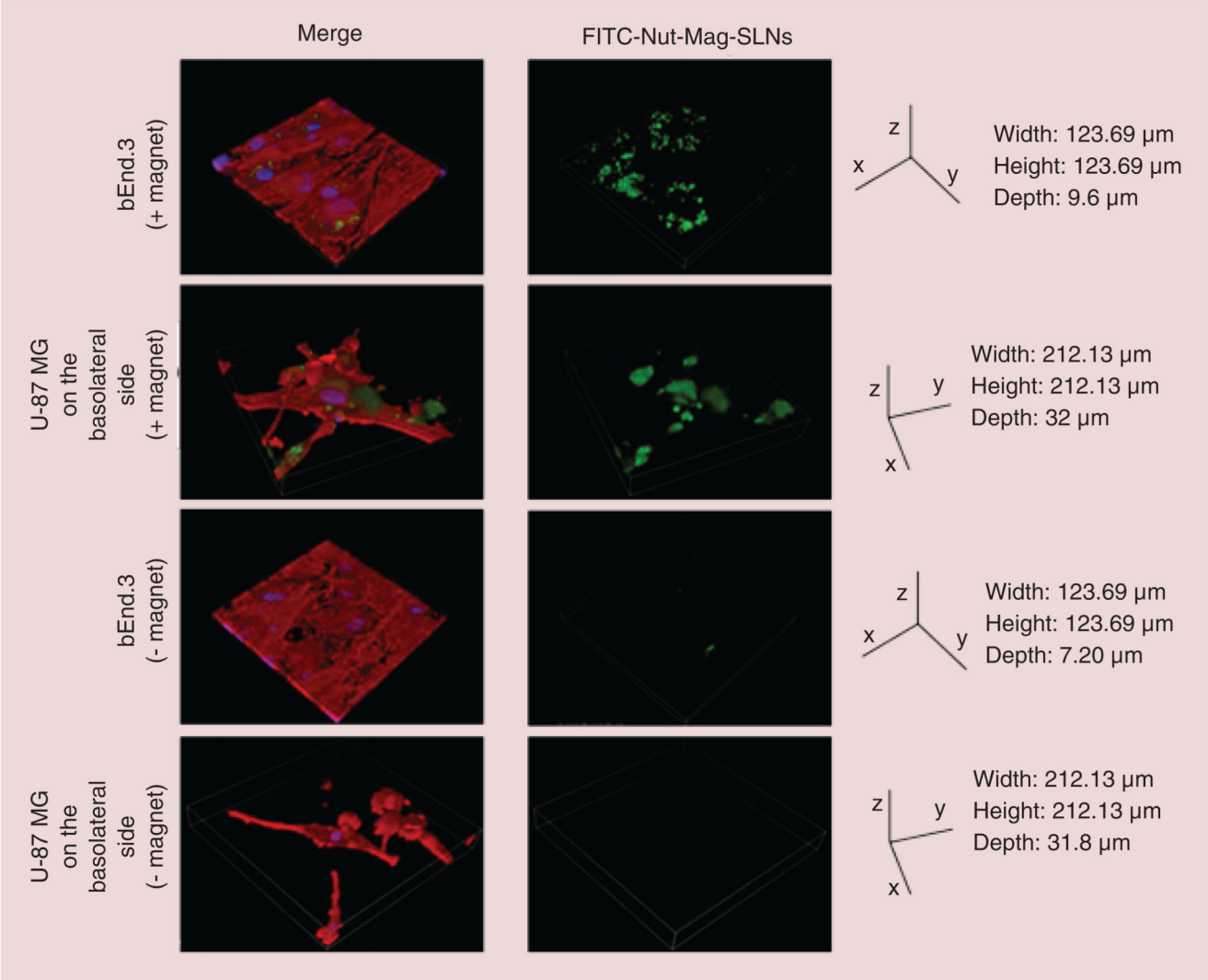

Figure 9. Confocal imaging after magnetic targeting of nutlin-loaded magnetic solid lipid nanoparticles.

3D rendering showing accumulation of Nut-Mag-SLNs and their internalization into bEnd.3 and U-87 MG cells after magnetic targeting experiment. FITC-Nut-Mag-SLNs in green, f-actin in red, nuclei in blue.

FITC: Fluorescein isothiocyanate; Nut-Mag-SLNs: Nutlin-loaded magnetic solid lipid nanoparticles.

Europe PMC Funders Author Manuscripts

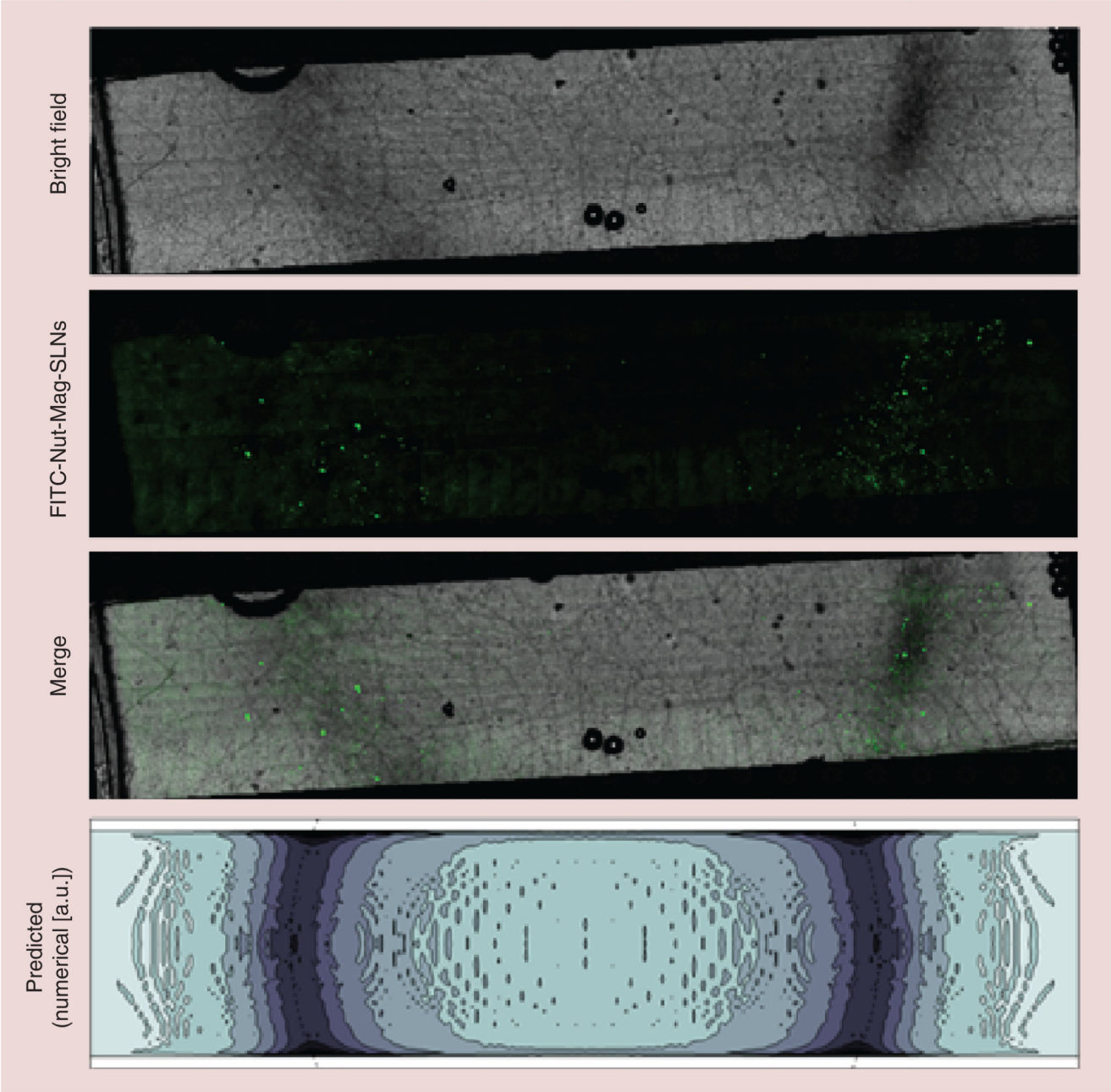

Figure 10. Distribution of FITC-nutlin-loaded magnetic solid lipid nanoparticles attracted by the external magnet onto the porous membrane.

Bright field acquisition (first row), fluorescence acquisition (second row) and merging (third row). Density contour plot (fourth row) of the captured FITC-Nut-Mag-SLNs, as predicted by the numerical model (the dashed line denotes the top edge of the underlying magnet). FITC: Fluorescein isothiocyanate; Nut-Mag-SLNs: Nutlin-loaded magnetic solid lipid nanoparticles.

Europe PMC Funders Author Manuscripts

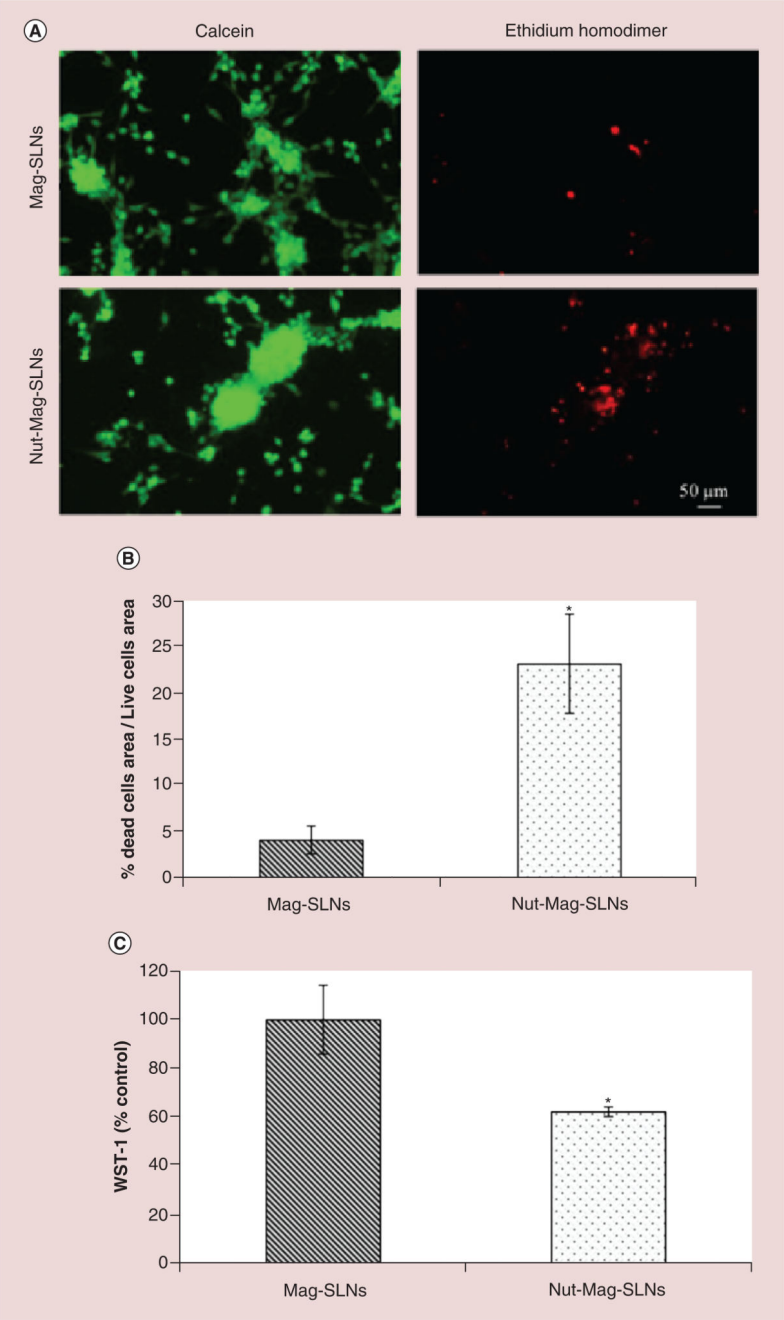

Figure 11. Nutlin-loaded magnetic solid lipid nanoparticles effects on the microfluidic blood–brain barrier model after magnetic targeting experiment.

(A) Results of the live/dead viability/cytotoxicity assay on U-87 MG cells following bEnd.3 monolayer crossing by Mag-SLNs and Nut-Mag-SLNs. **(B)** Ratio (expressed as %) between calcein and ethidium homodimer signal area. **(C)** Metabolic WST-1 assay of U-87 MG cells after bEnd.3 monolayer crossing by Mag-SLNs and Nut-Mag-SLNs.

*$p < 0.05$.

BBB: Blood–brain barrier; Mag-SLNs: Magnetic solid lipid nanoparticles; Nut-Mag-SNLs: Nutlin-loaded magnetic solid lipid nanoparticles.

Europe PMC Funders Author Manuscripts